Measurement and Correlation of Directional Permeability and Forchheimer's Inertial Coefficient of Micro Porous Structures Used in Pulse-Tube Cryocoolers

A Thesis
Presented to
The Academic Faculty

by

William M. Clearman

In Partial Fulfillment
of the Requirements for the Degree
Master of Science in Mechanical Engineering

Georgia Institute of Technology

August, 2007

Measurement and Correlation of Directional Permeability and Forchheimer's Inertial Coefficient of Micro Porous Structures Used in Pulse-Tube Cryocoolers

Approved by:

Dr. S. Mostafa Ghiaasiaan, Chair
School of Mechanical Engineering
Georgia Institute of Technology

Dr. Carl S. Kirkconnell
Space and Airborne Systems
Raytheon Company

Dr. Prateen V. Desai
School of Mechanical Engineering
Georgia Institute of Technology

Dr. Sheldon M. Jeter
School of Mechanical Engineering
Georgia Institute of Technology

Date Approved: June, 2007

ACKNOWLEDGEMENTS

Before presenting this thesis, I would first like to thank all of the individuals that contributed to its content. First of all, I'd like to thank my academic advisor, Dr. S. Mostafa Ghiaasiaan, for giving me the opportunity to work with and learn from him during my time at Georgia Tech. His tremendous knowledge and willingness to teach were invaluable to the completion of my studies and my overall graduate research experience. I'd also like to thank Dr. Carl S. Kirkconnell of Raytheon Company for his continued support of our research group. He has provided our research with the foundation and direction required to make a difference and without his contributions, none of this work would have been possible. I'd also like to thank Dr. Prateen V. Desai and Dr. Sheldon M. Jeter. As members of my graduate review committee, their insight and recommendations will be instrumental towards the successful completion of this project.

Perhaps most importantly, I'd like to personally thank Jeesung "Jeff" Cha for his constant guidance and endless patience throughout the past two years. More than any other person, Jeff was always around to answer questions and offer advice, suggestions, and constructive criticism and his contributions have been a vital part of this research project. I'd also like to thank Dr. Jeremy P. Harvey and Ted Conrad for all of their help and advice.

Outside of the academic world, I have relied on a number of other people for strength, support, and motivation. Most importantly, I want to thank my family who have all been the most positive of influences on my life. My father, Tom, and my mother, Marie, have worked tirelessly to give me and my brother, Matthew, opportunities that many people do not have and I cannot understate my appreciation for all they have sacrificed. Throughout our lives they have taught, encouraged, and supported us every

step of the way and I am forever grateful for all they have done for both of us. I'd also like to thank all my other friends and loved ones who have been there to not only keep me focused on my work, but also to provide me with an escape from it when I needed it most.

TABLE OF CONTENTS

LIST OF TABLES

LIST OF FIGURES

NOMENCLATURE

Variables:

A	Cross Sectional Area of Flow Tube (m^2)
c_f	Forchheimer Coefficient
C	Inertial Resistance (m^{-1})
C_p	Specific Heat Capacity (J/kg-K)
D	Viscous Resistance ($1/m^2$)
f	Friction Factor
FS	Full Scale Value
h	Convective Heat Transfer Coefficient (W/m^2)
k	Thermal Conductivity (W/m-K)
K	Permeability (m^2)
L	Length of Porous Zone (m)
P	Fluid Pressure (Pa)
$P_{critical}$	Fluid Critical Pressure (Pa)
q	Convective Heat Transfer (W)
R	Gas Constant (J/kg-K)
Re_K	Reynolds Number with $K^{1/2}$ as Length Scale
S_f^h	Fluid Enthalpy Source (W/m^3)
t	Time (s)
T	Temperature (K)
T_{ac}	Period (s)
u	Superficial Velocity (m/s)

v	Physical Velocity (m/s)
V_{total}	Volume of solid material and void space (m^3)
V_{void}	Volume of Void Space (m^3)
V_{solid}	Volume of Solid Material (m^3)
x	Axial Coordinate (m)

Greek Letters:

ε	Porosity
θ	Mass Flow/Pressure Phase Angle (rad)
μ	Fluid Dynamic Viscosity (N-s/m^3)
ρ	Density (kg/m^3)
σ	Uncertainty
$\bar{\bar{\tau}}$	Viscous Stress Tensor (Pa)

Notation and Symbols:

A_s	Surface Area of Solid Porous Matrix (m^2)
C_{ij}	Inertial Resistance Matrix (m^{-1})
C_p	Pressure Dependant Inertial Resistance (m^{-1})
D_{ij}	Viscous Resistance Matrix (m^{-2})
D_p	Pressure Dependant Viscous Resistance (m^{-2})
∇	Del Operator (m^{-1})
E_f	Total Specific Energy of Fluid (kJ/kg)
E_s	Total Specific Energy of Solid (kJ/kg)

P_d	Dynamic Pressure (kPa)
$\vec{F}$	External Body Force Vector (N/m^3)
F_i	External Body Force in the i^{th} direction (N/m^3)
$\vec{g}$	Gravitational Acceleration (m/s^2)
$\dot{H}$	Enthalpy Flow Rate (kW)
$\langle \dot{H} \rangle$	Time-Averaged Enthalpy Flow Rate (W)
$\bar{\bar{I}}$	Unit Tensor
J_i	Diffusion Flux of Species i (kg/m^{2}s)
$\dot{m}$	Mass Flow Rate of Working Fluid (kg/s or g/s)
ΔP	Pressure Drop (Pa)
∇P	Pressure Gradient (Pa/m)
∇T	Temperature Gradient (K/m)
T_0	Average Temperature (K)
T_∞	Bulk Fluid Temperature (K)
$\vec{v}$	Velocity Vector (m/s)
$\dot{V}$	Volumetric Flow Rate (m^3/s)

SUMMARY

Since the middle of the 20th century, an increasing demand in industry for smaller, colder, and more reliable and efficient cooling systems has led to an increase in research and development of alternatives to the widely-used vapor-compression refrigerator. For many modern applications, the need to obtain cryogenic temperatures lower than 120 K, or -153 °C, has surpassed the capability of traditional refrigeration systems and led to the advent of cryocooler refrigerators. Unlike their counterparts, many cryocoolers make use of oscillatory compression and expansion of gas in a closed system consisting of multiple components in order to remove heat from the desired environment. Upon reaching steady-state, these refrigerators have been shown to reach temperatures less than 1 K.

The ability of cryocoolers to effectively operate at such low temperatures has made them an integral part of many emerging areas of study related to cryogenics. Due not only to their cooling capacity, but also their compact design and reliability, these devices have become suitable for a large variety of applications spanning a wide range of industries including military, space, medical, environmental, and biological. Specifically, cryocoolers have been used for various applications including focal plane array cooling of infrared or thermal sensing systems, cooling of superconducting magnets used in Maglev trains and magnetic resonance imaging (MRI) technology, cryopumps used in the semiconductor fabrication industry, and liquefaction of air and many different gases.

Early in their development, the oscillatory nature of the flow within most cryocoolers was not well understood, but ongoing research and investigation into the behavior of these periodic-flow devices has led to numerous improvements of their design and greatly increased their applicability to a number of emerging technologies.

Since their inception, the desire to improve cryocooler performance and efficiency has been the main impetus for continued research development.

Currently, one area of consideration made possible by significant advances in computational capabilities involves the use of Computational Fluid Dynamics (CFD). CFD is the science of determining approximate numerical solutions to both the momentum and energy governing equations of fluid flow based on space and time. Historically, researchers have been limited to exact solutions of only a few classical flow problems where simplifying assumptions allowed them to be easily evaluated. Today, various CFD software packages utilize the growing computing power of modern computers to allow researchers to accurately predict solutions for entire flow fields of complex definition without making arbitrary simplifying assumptions.

One such application of CFD lies in the analysis of the cryocooler regenerator. Typically, a regenerator is a solid structure of micro porous material through which the cryogenic fluid will flow and exchange heat. It acts to pre-cool the working fluid during compression before it enters the cold heat exchanger. In this component, the characteristic dimension of the cryocooler becomes much smaller compared to the mean free path of the gas molecules so continuum-based governing equations can no longer be applied. As a result, analysis of the solid-fluid interaction of the flow within a cryocooler would be nearly impossible due to the scale and complexity of the solid-fluid interface. However, when provided with accurate closure relations for the volume-averaged governing equations, CFD has demonstrated a very promising ability to accurately simulate the flow through the regenerator and predict fluid behavior.

The objective of this investigation is to measure and empirically correlate the steady flow axial hydrodynamic parameters for some widely used cryocooler regenerator structures (325 and 400 stainless steel mesh, stainless steel metal foam, and perforated disks) at various porosities using CFD. A CFD model of the regenerator test section and

its vicinity was created and iteratively used along with experimental data to provide a solution of the governing conservation equations resulting in the determination of the permeability and Forchheimer coefficient associated with the individual regenerator fillers. Results from this investigation allow for direct comparison of the axial parameters to previously determined radial parameters in order to examine the effect of multi-dimensional flow within the regenerator and it allows for direct comparison of steady flow effects to periodic flow effects for identical micro porous structures. Also, the effect of varying pressure on the steady flow hydrodynamic parameters and friction factors were studied.

The results of this investigation were then used in cooperation with those of the corresponding radial and periodic flow investigations conducted by Cha *et al.* [21, 29] to determine the suitability of making some common simplifying assumptions about fluid flow through the cryocooler regenerator. Results indicate that assuming isotropic hydrodynamic parameters for flow through porous components with small aspect ratios, or using steady flow parameters to model a periodic system, could introduce significant error in predicting hydrodynamic losses. It was also shown that the permeability and Forchheimer Coefficient associated with steady 1-D compressible flow through porous media are functions of pressure as well as Reynolds number. While this research does involve micro porous materials used in pulse-tube cryocoolers, the conclusions presented in this thesis can generally be applied to flow through any porous medium.

CHAPTER 1

INTRODUCTION

The origin of the cryocooler dates back to the year 1815 when Robert Stirling first conceived what we now know as the Stirling engine as an alternative to the typical steam engines of the time. The Stirling engine is a closed system in which a working fluid moving between a hot heat exchanger, a regenerator, and a cold heat exchanger is repeatedly expanded and compressed by the addition and removal of heat which results in work done by a piston. Originally, the Stirling engine was used to produce power using heat exhausted from a furnace, but in 1874, Alexander Kirk first used the Stirling engine as a refrigerator by inputting work through the piston and absorbing heat from the desired environment through the cold end heat exchanger. [5]

1.1 The Stirling Refrigerator

Since 1956, after substantial research and development led by Jan Köhler of the Philips Company, various versions of the Stirling refrigerator (Figure 1) have been made available for commercial sale and have been applied to a number of industrial applications requiring cooling at cryogenic temperatures such as gas liquefaction [5]. During that time, there have been numerous advances in the design of these cryocoolers resulting in improved efficiency and lower cold end temperatures.

Figure 1: Stirling Cycle Miniature Refrigerator (www.janis.com)

Overall, the desired effect of the Stirling Refrigerator is to minimize the temperature at the cold end of the regenerative heat exchanger in order to maximize the time-averaged heat transfer into the system. To do this, we want to maximize the enthalpy flow away from the cold end and minimize the enthalpy flow towards the cold end. Following the compression process, the regenerator absorbs heat from the warm fluid moving through the porous matrix and stores it for one half-cycle thus reducing the enthalpy flow to the cold heat exchanger. For an ideal regenerator, all of the stored heat is then transferred back to the fluid as it is de-pressurized and moves back towards the warm heat exchanger where the heat is rejected. [6]

The fluid undergoes a regenerative cycle known as the Stirling Cycle (refer to Figure 3). (3-4) Ideally, the fluid is isothermally expanded and absorbs heat from the cooled environment. (4-1) A portion of this heat is then rejected, or stored, in the regenerator. (1-2) The working fluid is then isothermally compressed and rejects the remaining heat to the surroundings. (2-3) The fluid then absorbs the stored heat from the regenerator at constant volume and the cycle is complete.

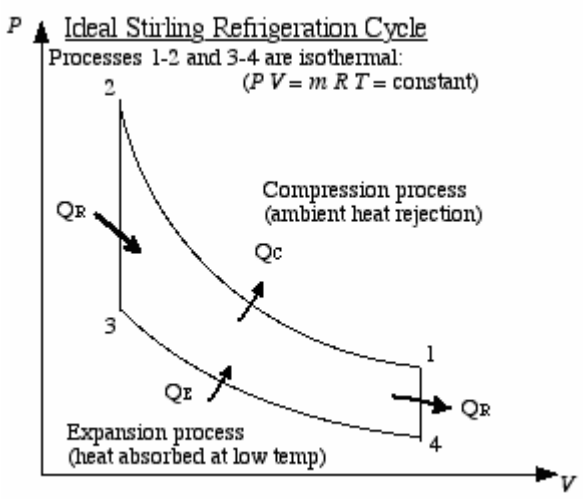

Figure 3: Ideal Stirling Refrigeration Cycle

In a commonly used approach, the regenerator matrix is made up of stacked, finely meshed screens made of woven wires or packed spheres in order to increase the solid surface area, A_s, and enhance convective heat transfer, q, with the working fluid according to Newton's Law of Cooling (Eq. 1):

$$q = hA_s(T_s - T_\infty) \qquad \text{(Eq. 1)}$$

where h is the convection heat transfer coefficient and T_s and T_∞ are the solid surface temperature and the bulk fluid temperature respectively. In most cases, helium is used as the working fluid in regenerative refrigeration cycles because of its high thermal conductivity and high specific heat ratio. Ideally, the regenerator matrix should be made of a material with an infinitely high thermal heat capacity (mass times specific heat capacity) compared to that of the working fluid in order to guarantee maximum regenerator effectiveness and reduce the debilitating effects of thermal saturation of the matrix [5]. The pressure drop across the regenerator, which is directly proportional to

the Reynolds number for laminar flow, also has a direct negative impact on the refrigeration capacity of the cryocooler and should be minimized in order to maximize P-V work in the cryogenic expansion space. Use of a large, open, highly porous regenerative matrix reduces pressure drop, but can also reduce heat transfer between the fluid and the matrix. Open regenerator designs also increase void space which reduces the thermal heat capacity of the matrix [5] and reduces desirable pressure oscillations for a given swept volume of the compressor piston [3]. Therefore, it is important to find the optimal balance between having both a low pressure drop and maximum heat transfer across the regenerator while minimizing void space in cryocooler design.

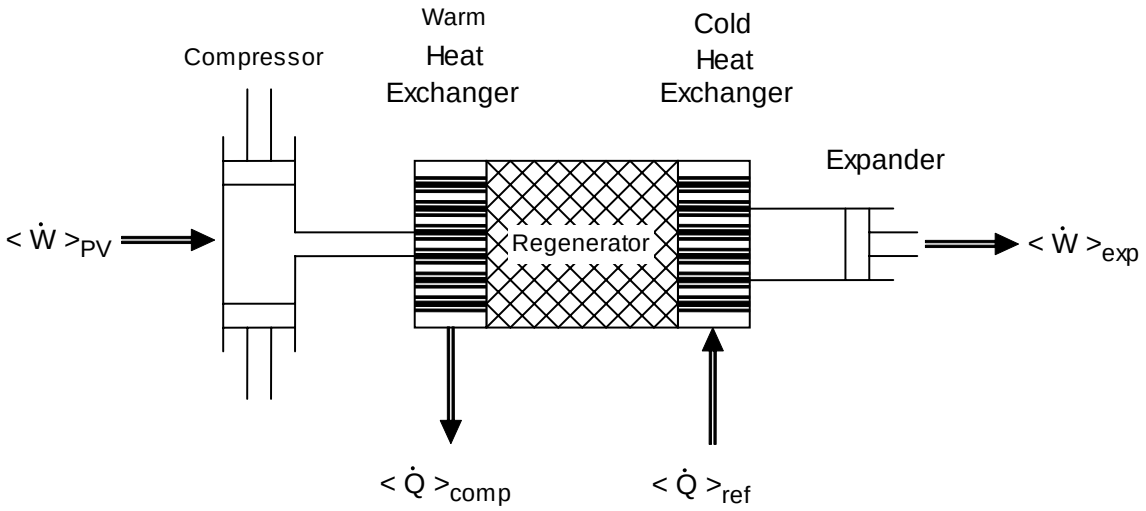

Figure 2: The Stirling Refrigerator

An important feature of the Stirling Refrigerator is the use of an expansion piston at the cold end (refer to Figure 2). The purpose of this expander is to control the expansion of the gas in order to optimize the phase angle between the mass flow rate and the fluid pressure [3]. Consider an ideal gas as the working fluid of the Stirling

Refrigerator. After cycle-averaging the general property relations by integrating the thermodynamic properties over the entire cycle and then dividing by the period, the cyclic averaged enthalpy flow, $\langle \dot{H} \rangle$, can be described by:

$$\langle \dot{H} \rangle = \frac{1}{T_{ac}} \oint \dot{m} C_p T dt \qquad \text{(Eq. 2)}$$

where $\dot{m}$ is the mass flow rate, T_{ac} is the period, C_p is the gas specific heat, and T is the gas temperature. It can be seen from Eq. 2 that in order to maximize the enthalpy flow, it is necessary to ensure that the oscillatory mass flow rate is in phase with the instantaneous fluid temperature, meaning that the maximum mass flow rate occurs at the same instant as the maximum temperature. For low flow rates, the gas can be assumed to be incompressible. Therefore, according to the ideal gas law:

$$P = \rho R T \qquad \text{(Eq. 3)}$$

the pressure, P, and the temperature, T, will be in phase if the density, ρ, is assumed to be constant. By adjusting the expander, the phase relationship between the mass flow rate and the gas pressure and temperature can be optimized which ultimately results in higher enthalpy flow, higher heat transfer, and a greater capacity to refrigerate. [4]

For higher flow rates, or flow through the regenerator where larger pressure and density gradients are present, Radebaugh has also demonstrated why it is desirable to have an in-phase relationship between the mass flow rate and the fluid pressure [3]. The time averaged enthalpy flow can also be written as a combination of the First and Second Laws of Thermodynamics:

$$\left\langle \dot{H} \right\rangle = \left\langle P_d \dot{V} \right\rangle + T_0 \left\langle \dot{S} \right\rangle \qquad \text{(Eq. 4)}$$

where $\left\langle P_d \dot{V} \right\rangle$ is the time-averaged acoustic power, P_d is the dynamic pressure, $\dot{V}$ is the volume flow rate, T_0 is the average temperature, and $\left\langle \dot{S} \right\rangle$ is the time-averaged entropy flow. For an ideal system lacking irreversibilities, the time-averaged entropy flow will be equal to zero and the time-averaged enthalpy flow will be equal to the acoustic power which, if it is a sinusoidal function of time, is:

$$\left\langle P_d \dot{V} \right\rangle = \frac{1}{2} P_1 \dot{V}_1 \cos\theta = \frac{1}{2} R T_\infty \dot{m}_1 \left(\frac{P_1}{P_\infty} \right) \cos\theta \qquad \text{(Eq. 5)}$$

Equation 5 demonstrates why particular care is taken in the design of cryogenic refrigerators to ensure a minimum phase difference, θ, between the mass flow rate and the fluid pressure at a point, P_1, so that maximum enthalpy flow away from the cold heat exchanger can be achieved.

While the use of an expansion piston is often desirable because it increases the performance of the refrigerator, it does present some problems for certain applications. The additional moving part makes the device less reliable and also contributes unwanted vibrations. For applications like those used in satellites, where long life and smooth operation is vital, the Stirling Cryocooler is not always the best choice of refrigerator.

1.2 The Basic Pulse Tube Refrigerator

In 1964, Gifford and Longsworth first proposed the use of a pulse tube to enhance the performance of cryocoolers [1]. In place of the expansion piston, they attached a tube and an additional heat exchanger to the cold end of the refrigerator. This alternative design is a more reliable and durable cryocooler with no moving parts at the cold end. Through a process called “surface heat pumping,” the periodic pressurization and depressurization of working fluid ultimately results in a hot end and a cold end of the pulse tube with heat being continuously pumped from the cold end to the hot end [2]. The result of these additional components is the Basic Pulse Tube Refrigerator (BPTR). While the BPTR was more reliable and tended to reduce vibrations, the removal of the expander prevented the optimization of the mass-pressure phase difference and greatly reduced the overall efficiency of the refrigerator.

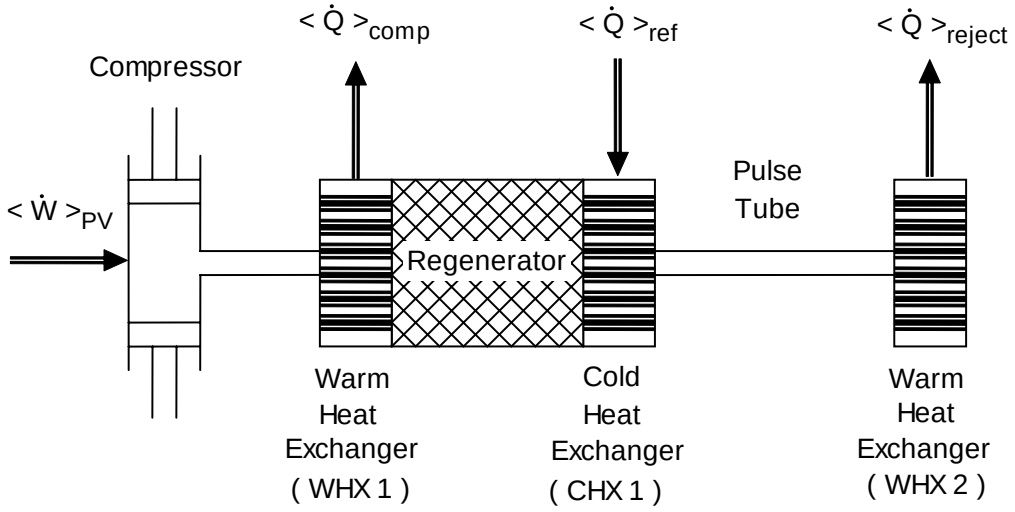

Figure 4: Basic Pulse Tube Refrigerator

1.3 The Orifice Pulse Tube Refrigerator

In 1984, Mikulin *et al.* improved the BPTR by introducing an orifice valve inside the pulse tube and a surge volume which was successful in slightly improving the thermodynamic efficiency and the useful refrigeration load [7]. One year later, Radebaugh *et al.* modified this design by moving the orifice valve outside the pulse tube on the other side of the warm heat exchanger (refer to Figure 5) [8]. Reaching temperatures as low as 60 K, the new Orifice Pulse Tube Refrigerator (OPTR) was an improvement over the BPTR because the addition of the orifice valve allowed for some adjustment of the flow for more optimal phase difference with the pressure oscillations. However, the added void volume and an undesirable pressure drop across the valve served to lower the pressure oscillations resulting in an overall efficiency of the OPTR that was still significantly less than that of the Stirling Refrigerator.

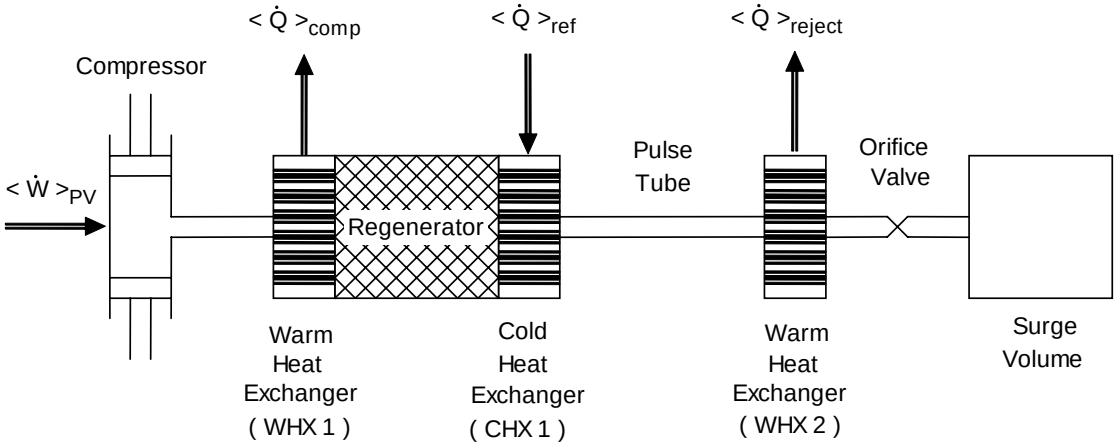

Figure 5: Orifice Pulse Tube Refrigerator

1.4 The Inertance Tube Pulse Tube Refrigerator

In an effort to further improve to performance of OPTRs, Zhu *et al.* presented their findings on the desirable effect of “long neck tubes” on the phase between the mass flow and the pressure in 1996 [10]. In the years that followed, Gardner and Swift recognized that useful work is dissipated as wasted heat at the orifice of the OPTR and that replacing the orifice valve with an inertance tube allows for the reduction of the surge volume and possibly the increase of the pulse tube volume and overall system performance [11]. This conclusion was verified by Roach and Kashani in 1997 when their detailed computer models demonstrated that Inertance Tube Pulse Tube Refrigerators (ITPTR) perform dramatically better than OPTRs [9].

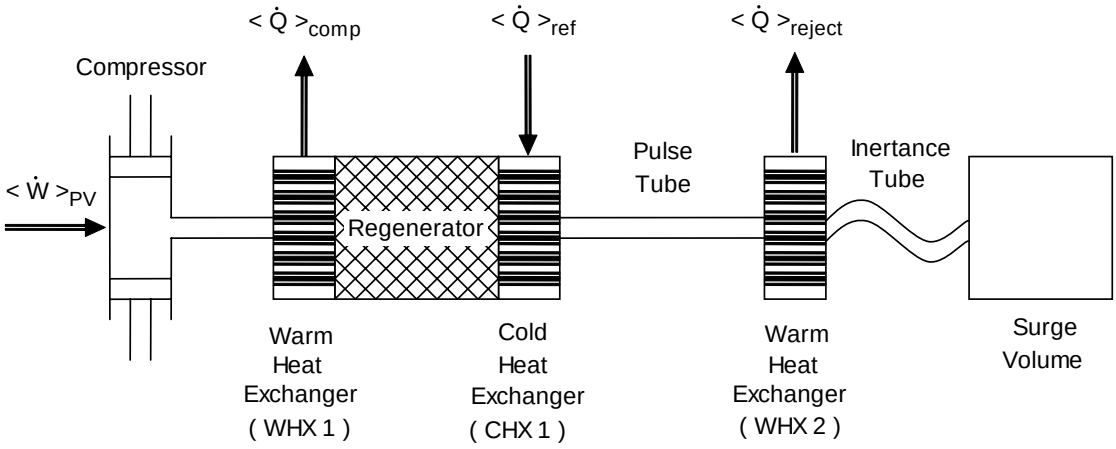

Figure 6: Inertance Tube Pulse Tube Cryocooler

CHAPTER 2

REVIEW OF MODERN CRYOCOOLER RESEARCH AND THEORY

Today, there remains a great deal of interest in further improving the understanding of the various types of cryocoolers on a system level as well as improving the performance of the individual components of these refrigerators. From a thermodynamic perspective, there will always be irreversibilities associated with any real system which detract from its ability to operate at the theoretical maximum efficiency, or Carnot Efficiency. For pulse tube refrigerators, these sources of irreversibility, or entropy production, include the following: hydrodynamic and thermodynamic losses across the heat exchangers and the regenerator, regenerator thermal inefficiency or low regenerator effectiveness, viscous dissipation, undesirable heat transfer across finite temperature gradients, and turbulent mixing [12]. With the total rate of entropy generation for the cryocooler being the sum of the irreversibilities of its components, it is important to identify the components where these losses tend to dominate and can be most easily minimized in order to improve the overall system level performance.

2.1 The Cryocooler Regenerator

The regenerator is typically the largest source of loss mechanisms which adversely effect cryocooler performance [18]. Axial heat conduction within the regenerator matrix, thermal saturation, and frictional losses all inhibit the refrigerator's ability to operate with maximum efficiency. There is a substantial amount of current research dedicated to the improvement of regenerators by focusing on a few key topics

like material selection, regenerator structure, and methods of analysis of fluid flow through porous media. [13]

The proper choice of regenerator material can have a very big impact on the overall cryocooler performance. It is important that regenerator material have a very high thermal heat capacity. Typically, stainless steel is selected for its resistance to corrosion, high specific heat capacity, and relatively low thermal conductivity, but for a cryocooler application, the large temperature difference between the cold end and the hot end of the regenerator matrix can cause orders of magnitude variation in the thermal properties of the material along its length which can significantly effect performance at very low temperatures [13]. A number of recent studies investigate the use of various materials like erbium and titanium alloys which have more favorable thermal properties at very low temperatures [14, 15]. However, cost and difficulty producing these alloys as well as decreased ductility limits their use. There are also recent investigations into the use of “textile type” regenerators made of interwoven ceramic fibers, stainless steel wire, and fine threads which have shown promise of increasing heat transfer while reducing pressure drop [25].

Regenerator structure, or geometry, also plays an important role in cryocooler design. Ideally, the axial conduction of heat should be as small as possible in order to minimize enthalpy flow to the cold region of the cryocooler while the radial conduction should be as large as possible to prevent thermal saturation of the solid matrix [16]. The matrix structure should also minimize hydrodynamic losses of the fluid flow. In industry, a majority of regenerators are made of stacks of fine mesh screens made of conductive material. However, packing of these screens has to be done very carefully and can often be very time consuming. There are a number of investigations into the use of tightly packed spheres, perforated disks, sintered mesh screens, and metal foams where

the optimal balance between desired thermal and hydrodynamic characteristics is sought [13, 17].

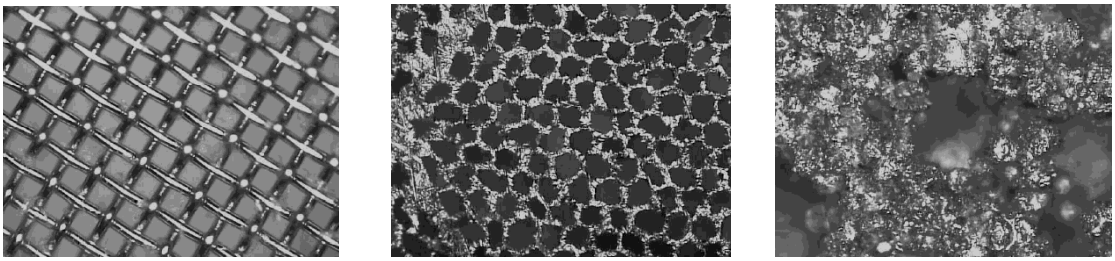

(a) (b) (c)

Figure 7: Porous Materials Under Magnification: (a) Wire Mesh Screen - 200x, (b) 60 μm Perforated Disk - 200x, (c) Metallic Foam - 200x (from [13])

Due to the complex and micro porous nature of the regenerator matrix, classical methods of solving the governing equations become impossible. Recent investigations have shown that CFD tools can be very useful towards the design and optimization of various cryocooler components by providing detailed information about the flow field and thermodynamic processes that would be impractical to obtain experimentally. Historically, the analysis of the ideal regenerator consisted of the following assumptions: heat stored in the fluid is small compared to the thermal capacity of the matrix, fluid flow is one-dimensional and in the axial direction only, axial thermal conductivity is zero and radial conductivity is infinite, and fluid and regenerator properties are constant and do not vary with temperature [16]. The advent of CFD to solve the volume-averaged governing equations has allowed investigators to accurately simulate a large number of different regenerator configurations and led to a number of important realizations which have helped engineers improve regenerator design and select appropriate simplifying assumptions more representative of an actual refrigeration system. For example, Hou

et al. recently utilized a numerical simulation to maximize the performance of a miniature pulse tube refrigerator by optimizing the ratio of the void volume of the regenerator to the swept volume of the compressor. This one-dimensional numerical model was verified against experimental data and indicated an optimal ratio to reduce pressure drop while maximizing heat capacity in the range of 1.0 to 1.2. [26]

In another recent study, Cha used CFD to demonstrate the effect of multi-dimensionalities on pressure drop, dissipation, and heat transfer processes in the porous regenerator [4]. He concluded that analysis based on the assumption of one-dimensional flow is inadequate for a system with one or more components having small length-to-diameter ratios, or aspect ratios. Also, Nam and Jeong demonstrated that the operating frequency of the cryogenic refrigerator has a substantial impact on the fluid flow-pressure phase difference and thus the cryocooler effectiveness and concluded that using steady flow hydrodynamic parameters to analyze periodic systems like the cryocooler provides an inaccurate description of system behavior [20]. Jeong *et al.* also note that the maximum friction factor of oscillating flow at high frequency can be significantly different from the friction factor determined for steady flow [22]. It is the objective of this investigation to use CFD to verify these assertions by providing a numerical analysis of hydrodynamic regenerator behavior under steady flow conditions and comparing results to previously documented periodic and multi-dimensional flow analyses.

2.2 Porous Media Flow Theory

Analysis of the regenerator requires an understanding of porous media flow and the equations governing the hydrodynamic and thermodynamic processes. The porosity, ε, of a porous region is defined by Eq. 6.

$$\varepsilon = \frac{V_{void}}{V_{total}} = 1 - \frac{V_{solid}}{V_{total}} \qquad \text{(Eq. 6)}$$

The total volume of the porous region, V_{total}, is the sum of the volume of the solid material, V_{solid}, and the volume of the void space, V_{void}. Therefore, fluid flow becomes less restricted and its physical velocity, v, is decreased relative to its superficial velocity, u, as the porosity approaches unity. The superficial velocity is the velocity of the fluid outside of the porous region and is related to the physical velocity, or the actual velocity inside the porous region, by the porosity.

$$u = \varepsilon v \qquad \text{(Eq. 7)}$$

In 1856, hydrologist Henry Darcy experimentally derived the following relationship between fluid velocity, u, and change in pressure, ΔP, for steady-state unidirectional flow of an incompressible substance through porous media:

$$\frac{\Delta P}{L} = \left(\frac{\mu}{K}\right) u \qquad \text{(Eq. 8)}$$

where μ is the fluid's dynamic viscosity and K is the permeability of the medium. Known as Darcy's Law, Eq. 8 states that the unidirectional pressure drop of a fluid flowing steadily through a porous medium is linearly proportional to the flow rate. The

permeability, K, has units of length squared and is independent of the nature of the flow. It is a statement of surface drag due to friction and is a function of the medium that can vary greatly depending on the morphology of the material used as the porous volume filler. [23]

Recognizing that inertial and form drag effects resulting from the physical obstruction of flow imposed by the solid matrix geometry become more dominant as flow velocity is increased, Darcy's Law was modified a number of times by a number of researchers. One of the more accepted modifications known as the Forchheimer Equation incorporates an additional term which corrects Darcy's Law at high flow speeds where inertial effects are more prevalent:

$$\frac{\Delta P}{L} = \underbrace{\frac{\mu}{K}u}_{DarcyTerm} + \underbrace{\frac{\rho c_f}{\sqrt{K}}u^2}_{ForchheimerTerm} \qquad \text{(Eq. 9)}$$

The additional term contains the permeability, K, the fluid density, ρ, and the dimensionless drag coefficient or Forchheimer's inertial coefficient, c_f, which is a function of the porous matrix geometry and the bounding walls of the regenerator. This correction accounts for the pressure drop's deviation from linearity as the Reynolds number of the fluid flow increases. The Forchheimer Equation can also be re-written (Eq. 10) in terms of the mass flow rate, $\dot{m}$, and the cross sectional area of the flow tube, A, using the relation given by Eq. 11.

$$\frac{\Delta P}{L} = \underbrace{\frac{\mu}{K\rho A}\dot{m}}_{DarcyTerm} + \underbrace{\frac{c_f}{\sqrt{K}\rho A^2}\dot{m}^2}_{ForchheimerTerm} \qquad \text{(Eq. 10)}$$

$$\dot{m} = \rho A u \qquad \text{(Eq. 11)}$$

An important note is that for a Reynolds number (Eq. 12) of order unity or smaller, the linear Darcy Term tends to dominate the pressure drop while for a high Reynolds number, the quadratic Forchheimer term tends to dominate.

$$\mathrm{Re}_K = \frac{\rho u K^{1/2}}{\mu} = \frac{\dot{m} K^{1/2}}{A\mu} \qquad \text{(Eq. 12)}$$

Typically, the transition between the Darcy regime, where viscous effects dominate, to the Forchheimer regime, where inertial effects dominate, for unidirectional isothermal flow occurs in the Re_K range 1 to 10, where the Reynolds number uses the square root of the permeability, $K^{1/2}$, as the length scale [23].

Although the Forchheimer Equation was originally derived experimentally, it has since been theoretically developed more rigorously by Whitaker [24]. Whitaker used the method of volume-averaging of the governing Navier-Stokes equations for a Newtonian fluid along with relevant closure problems to determine the permeability tensor and the Forchheimer correction tensor for a spatially periodic representative volume of the porous medium. Due to the complex nature of the porous matrix, it becomes impossible to accurately define the boundary conditions required to solve the governing equations at the point scale. However, for a periodic representative volume of the porous medium, average values of the relevant parameters across the entire volume can be used along with the volume-averaged conservation equations in order to obtain an approximate solution for the flow field. The reader may also refer to the “Handbook of Porous Media” for details on deriving the volume-averaged conservation equations [28].

Most present work applies volume-averaging of the fundamental hydrodynamic and energy equations to flow in porous media. However, in doing so, some information is lost and certain empirical relations need to be developed in order to solve the governing system of equations. Specifically, the permeability, K, and Forchheimer's inertial coefficient, c_f, need to be determined experimentally in order to close and numerically solve the system.

2.3 Computational Fluid Dynamics

Current trends in research show an increased use of computational fluid dynamics tools to determine numerical solutions to both the momentum and energy governing equations of fluid flow based on space and time. CFD programs like Fluent allow researchers to solve the volume-averaged conservation equations that govern fluid flow without making any unnecessary simplifying assumptions. This capability becomes especially valuable when seeking complete solutions for flow fields of complex definition like flow through micro porous media. Using Fluent, it is possible to create a model of flow through the porous cryocooler regenerator and, after defining the appropriate boundary conditions, numerically approximate the value of the desired hydrodynamic parameters.

For all flows, Fluent completely solves the relevant conservation equations without neglecting any terms within these equations. In this investigation, both the conservation of mass equation (Eq. 13) and the conservation of momentum equation (Eq. 14) will be volume-averaged and used to determine the permeability and Forchheimer coefficient for the porous material under investigation without making any unnecessary simplifying assumptions.

$$\frac{\partial \rho}{\partial t} + \nabla \cdot (\rho \vec{v}) = 0 \qquad \text{(Eq. 13)}$$

$$\frac{\partial}{\partial t}(\rho \vec{v}) + \nabla \cdot (\rho \vec{v} \vec{v}) = -\nabla P + \nabla \cdot \bar{\bar{\tau}} + \rho \vec{g} + \vec{F} \qquad \text{(Eq. 14)}$$

The stress tensor, $\bar{\bar{\tau}}$, is given by

$$\bar{\bar{\tau}} = \mu \left[\left(\nabla \vec{v} + \nabla \vec{v}^{T} \right) - \frac{2}{3} \nabla \cdot \vec{v} \bar{\bar{I}} \right] \qquad \text{(Eq. 15)}$$

Assuming isotropic porosity, ε, and single phase flow, the volume-averaged mass and momentum conservation equations to be solved by Fluent become:

$$\frac{\partial (\varepsilon \rho)}{\partial t} + \nabla \cdot (\varepsilon \rho \vec{v}) = 0 \qquad \text{(Eq. 16)}$$

$$\frac{\partial (\varepsilon \rho \vec{v})}{\partial t} + \nabla \cdot (\varepsilon \rho \vec{v} \vec{v}) = -\varepsilon \nabla P + \nabla \cdot (\varepsilon \vec{\tau}) + \varepsilon \vec{g} + \vec{F} \qquad \text{(Eq. 17)}$$

The external body force term, $\vec{F}$, accounts for viscous and inertial losses of the fluid within the porous media and is defined by Fluent as:

$$F_i = -\left(\sum_{j=1}^{3} D_{ij} \mu v_j + \sum_{j=1}^{3} C_{ij} \frac{1}{2} \rho v_{mag} v_j \right) \qquad \text{(Eq. 18)}$$

where F_i is the external body force term for the ith momentum equation, D is the viscous resistance matrix and C is the inertial resistance matrix as defined by Fluent. This external body force term is the drag force imposed by the pore walls and contributes to the pressure drop across the regenerator matrix. It is proportional to the fluid's physical velocity, v.

Therefore, for a homogeneous matrix with steady flow only and no internal axial body forces, the axial pressure drop as defined by Fluent becomes:

$$\frac{\partial(\varepsilon P)}{\partial x} = \underbrace{-\frac{\partial}{\partial x}(\varepsilon \rho v_i v_i)}_{\substack{Convective \\ Acceleration}} + \underbrace{\frac{\partial(\varepsilon \tau_i)}{\partial x}}_{\substack{Viscous \\ Stress}} - \left(\underbrace{D\mu v_i}_{\substack{Darcy \\ Term}} + \underbrace{\frac{C}{2}\rho v_{mag} v_i}_{\substack{Forchheimer \\ Term}} \right) \qquad \text{(Eq. 19)}$$

When Eq. 19 is compared to the Forchheimer Equation (Eq. 9), the similarities become evident. The Forchheimer Equation neglects the convective acceleration and the viscous stress term, or Brinkman Effect. Previous researchers have assumed that one or more of the terms in Eq. 19 have a negligible effect on the pressure drop across porous media. Therefore, their inclusion into the governing equation solved by Fluent provides the user with a solution more accurate relative to actual steady flow behavior than was possible before the advent of CFD.

By comparing Eq. 19 to Eq. 9, it can be shown that the viscous resistance term (from Eq. 18) is related to the permeability by

$$D = \frac{\varepsilon^2}{K} \qquad \text{(Eq. 20)}$$

and the inertial resistance is related to the permeability and the Forchheimer coefficient by

$$C = \frac{2\varepsilon^3 c_f}{\sqrt{K}} \qquad \text{(Eq. 21)}$$

The bracketed term on the right side of Eq. 19 can also be written in terms of a dimensionless friction factor, f, for convenience in quantifying viscous and inertial effects as function of the dimensionless Reynolds number as defined by Eq. 12:

$$D\mu v + \frac{C}{2}\rho v^2 = \frac{f}{2} D^{1/2} \rho v^2 \qquad \text{(Eq. 22)}$$

$$f = \frac{2\mu D^{1/2}}{\rho v} + \frac{C}{D^{1/2}} = \frac{2\varepsilon}{\mathrm{Re}_K} + 2c_f \varepsilon^2 \qquad \text{(Eq. 23)}$$

where v is the axial physical velocity of the working fluid.

In order to account for the temperature dependence of the fluid properties and the compressibility of the working fluid, it is also necessary for Fluent to solve the energy conservation equation:

$$\frac{\partial}{\partial t}(\rho E) + \nabla \cdot \left(\vec{v}(\rho E + P)\right) = -\nabla \cdot \left(\sum_j h_j J_j \right) + S_h \qquad \text{(Eq. 24)}$$

For flow through porous material, Fluent modifies the conduction flux and transient terms of the energy equation and solves Eq. 25.

$$\frac{\partial}{\partial t}\left(\varepsilon\rho_f E_f + (1-\varepsilon)\rho_s E_s\right) + \nabla\cdot\left(\vec{v}\left(\rho_f E_f + P\right)\right) = \nabla\cdot\left[k_{eff}\nabla T - \left(\sum_i h_i J_i\right) + \left(\bar{\bar{\tau}}\cdot\vec{v}\right)\right] + S_f^h \quad \text{(Eq. 25)}$$

where E_f is the total fluid energy, E_s is the total solid medium energy, k_{eff} is the effective thermal conductivity of the medium as defined by Eq. 26, J_i is the diffusion flux of species i, and S_f^h is the fluid enthalpy source term.

$$k_{eff} = \varepsilon k_f + (1-\varepsilon)k_s \quad \text{(Eq. 26)}$$

where k_f is the fluid thermal conductivity and k_s is the solid matrix conductivity.

CHAPTER 3

EXPERIMENTAL METHOD

Many modern CFD tools use the volume-averaged conservation equations to model porous media flow. As mentioned previously, in order to obtain a useful solution to these governing equations, the permeability and inertial coefficient first need to be accurately determined. Since these parameters are functions of the working fluid, the regenerator matrix, and the operating state of the cryocooler, it is not possible to obtain a universal relationship encompassing all of the many regenerator configurations in use. Currently, there is no comprehensive documentation of the permeability and inertial coefficient for different flow regimes, so they need to be determined for many different cryocooler regenerator designs on a case-by-case basis.

By designing a simple test apparatus capable of measuring the axial pressure drop for steady flow across a desired porous sample, it was possible to utilize CFD tools to determine the viscous resistance, D, and the inertial resistance, C, given a known flow rate of helium gas. After taking measurements, the pressure drop across the regenerator was plotted as a function of fluid mass flow rate and a fifth order polynomial curve of the form

$$\Delta P = a\dot{m}^5 + b\dot{m}^4 + c\dot{m}^3 + d\dot{m}^2 + e\dot{m} \qquad \text{(Eq. 27)}$$

was then fit to the data using the least-squares method. Then the mass flow rate and the recorded outlet pressure of a representative subset of the experimental data were used as boundary conditions for a Fluent model of the regenerator test section and the viscous resistance, D, and inertial resistance, C, as defined by Fluent were adjusted until

the simulated pressure drop across the entire test section most closely matched the average experimental pressure drop for the entire range of mass flow rates. Typical cryocoolers of interest to the current investigation operate between 0 g/s (gram/s) and 1.5 g/s so this study was focused only on flow rates within this range.

Once there was acceptable agreement between the experimental and simulated pressure drop across the porous test section, the permeability and the Forchheimer coefficient were then calculated using Eq. 20 and Eq. 21 and then correlated in terms of dimensionless parameters f and Re_K.

3.1 Experimental Objective

The objective of this investigation is to measure and empirically correlate the steady flow axial hydrodynamic parameters for candidate cryocooler regenerator structures. A test section was designed, constructed, and instrumented for the measurements and porous structures tested include 325 mesh and 400 mesh stainless steel screens at 69.69% porosity, sintered 400 mesh stainless steel screens at 61.65% porosity, stainless steel foam metal at 55.47% porosity, and stacked perforated disks at 26.8% porosity.

Tests were performed with helium as the working fluid and the longitudinal permeabilities and Forchheimer inertial coefficients were obtained using an iterative process where agreement between the data and the predictions of detailed CFD simulations for the entire test section were sought. Empirical correlations representing the longitudinal permeability and Forchheimer coefficient in terms of relevant dimensionless parameters were then developed and are reported in this thesis.

3.2 Experimental Apparatus and Procedures

In order to measure the steady flow axial pressure drop of helium gas through a porous regenerator sample, a simple experimental apparatus was designed and instrumented (refer to Figure 8). A line of compressed helium was run from a source tank through a pressure regulator and connected to the regenerator test section. Two high frequency Paine Electronics pressure transducers (Series 210-10) with an accuracy of 0.25% of their full scale were calibrated for pressures of up to 400 psia (2757 kPa) and were used to measure the fluid pressure just before and after the regenerator test section. A Sierra Instruments analog mass flow meter (Model 826 Toptrak) with an accuracy of 1.5% of its full scale (1.5 g/s) and calibrated at atmospheric conditions was connected after the test section and used to measure the helium mass flow rate at ambient pressure.

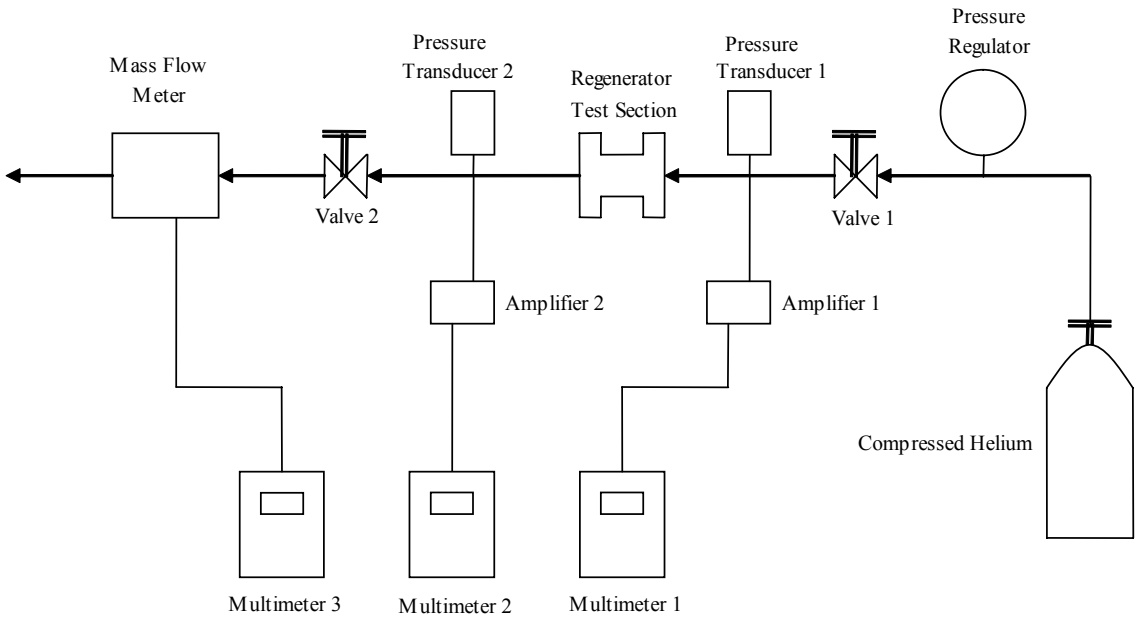

Figure 8: Axial Pressure Drop Experimental Apparatus Diagram

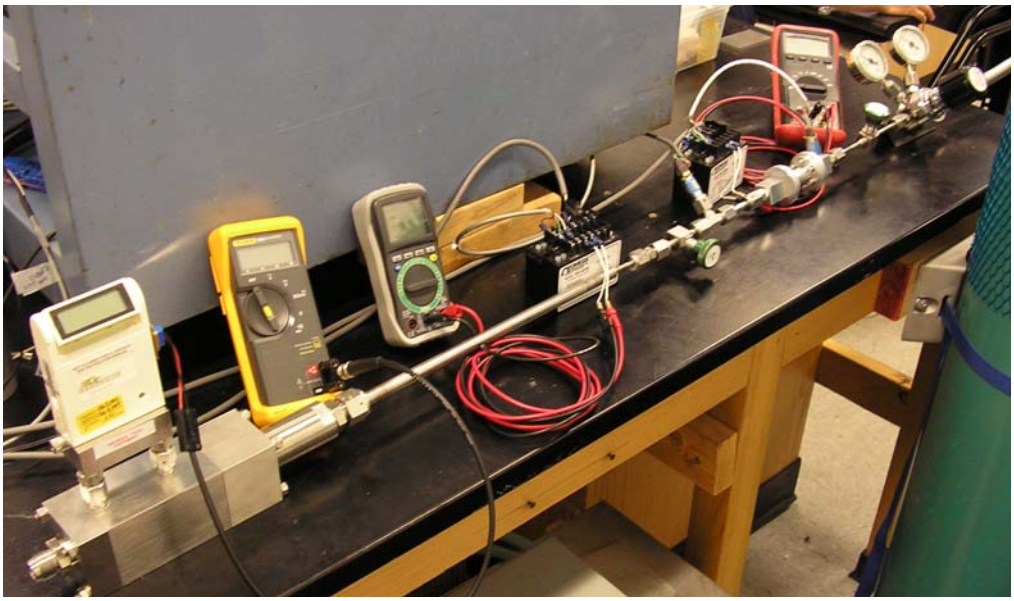

Figure 9: Axial Pressure Drop Experimental Apparatus

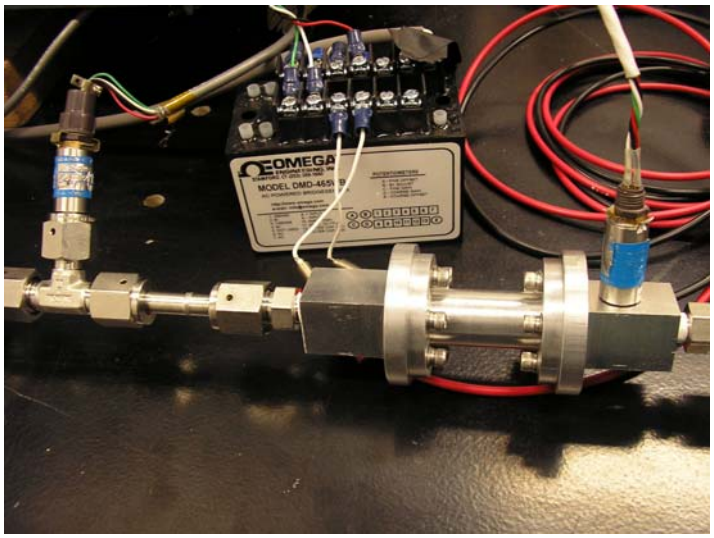

Figure 10: Regenerator Test Section

The regenerator test section is a slight variation of the design used by Cha [29]. Figures 11, 12, and 13 show detailed drawings of the test section and its vicinity. It is

made of aluminum 6061 and consists of the regenerator housing containing a 5/16” (0.794 cm) diameter by 1.5” (3.81 cm) length open volume for the porous test samples as well as two end pieces to hold the regenerator material in place. A larger regenerator housing 0.59” (1.499 cm) in diameter and 1.236” (3.139 cm) in length was used for the perforated disk samples.

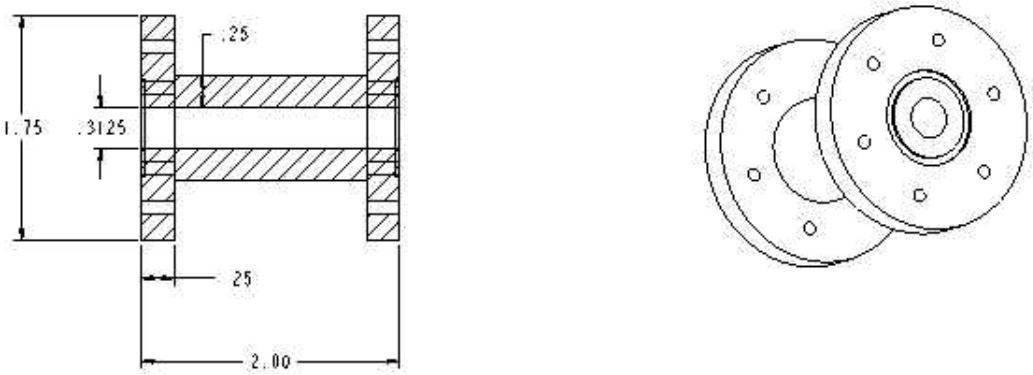

Figure 11: Detailed Regenerator Housing Drawing (Dimensions in Inches)

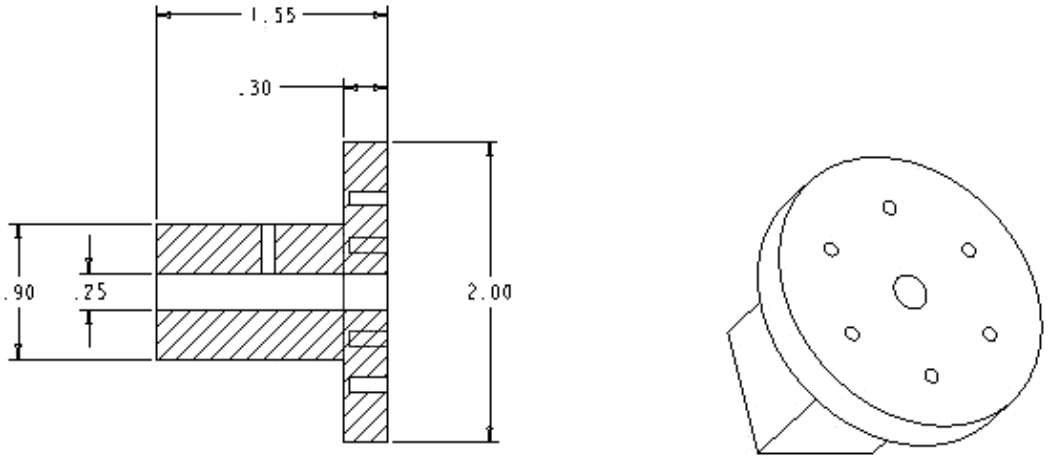

Figure 12: Detailed Left End Piece Drawing (Dimensions in Inches)

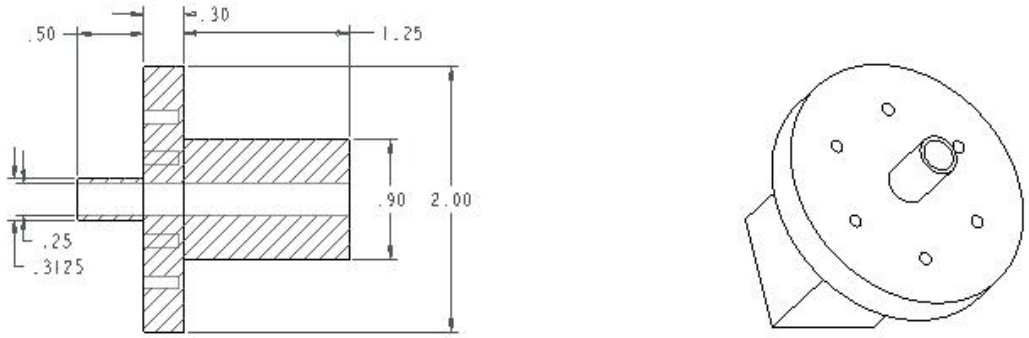

Figure 13: Detailed Right End Piece Drawing (Dimensions in Inches)

The regenerator housing was carefully packed with the desired regenerator material at the desired porosity and special care was taken to ensure that the apparatus was leak tight prior to testing. The regulator was set to 300 psia (2068 kPa) of pressure with valve 1 completely open and valve 2 completely closed. As valve 2 was slowly opened, fluid flow was initiated and the voltage outputs for multimeters 1, 2, and 3 were recorded and converted to the corresponding values of inlet pressure, outlet pressure, and mass flow. Experimental data were recorded for five different regenerator matrix samples (325 mesh and 400 mesh stainless steel screens both at 69.69% porosity, sintered 400 mesh stainless steel screens at 61.65% porosity, stainless steel foam metal at 55.47% porosity, and stacked perforated nickel disks at 26.8% porosity) for a range of flow rates between 0 g/s to 1.5 g/s. Refer to Appendix A for complete experimental procedures.

3.3 Experimental Results and Analysis

This section provides the results and complete analysis of the axial pressure drop data recorded for the different porous structures. The following are plots of the steady flow pressure drop across the regenerator test section versus the indicated mass flow rate of helium gas. Refer to Appendix B for complete tabulated data.

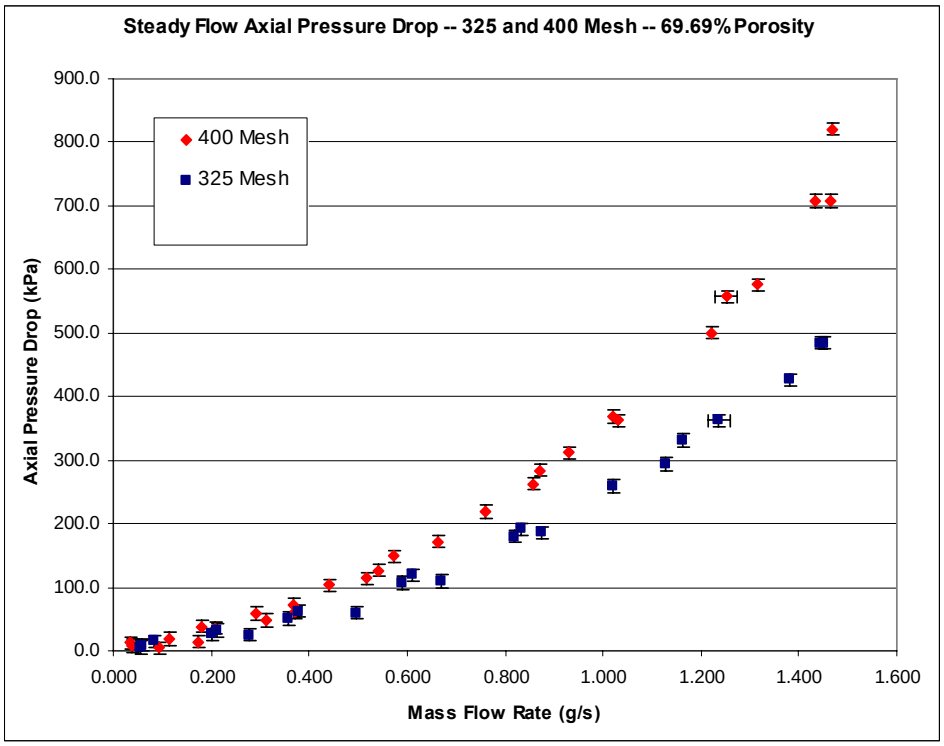

Figure 14: Steady Flow Axial Pressure Drop for 325 and 400 Mesh

Figure 14 demonstrates that, while the porous samples were of equal porosity, the finer 400 mesh screens provided a higher resistance to the flow and resulted in a higher pressure drop. At low flow rates, where viscous effects tend to dominate, the quasi-linear relationship between the pressure drop and the indicated mass flow rate can

be clearly seen. Likewise, at higher flow rates, inertial effects tend to dominate and the trend begins increasing in proportion to the flow rate squared.

The total error, $\sigma_{dP,total}$, associated with the pressure drop measurements equaled ±9.8 kPa and was calculated based on the uncertainties of the two pressure transducers, σ_1 and σ_2.

$$\sigma_{dP,total} = \sqrt{\sigma_1^2 + \sigma_2^2} \quad \text{(Eq. 28)}$$

$$\sigma_1 = 0.0025 FS_1 \quad \text{(Eq. 29)}$$

$$\sigma_2 = 0.0025 FS_2 \quad \text{(Eq. 30)}$$

where FS_1 = FS_2 = 400 psia (2757.6 kPa). The error associated with the indicated mass flow rate, $\sigma_{\dot{m}}$, is equal to ±0.0225 g/s or 1.5% of the mass flow meter's full scale of 1.5 g/s.

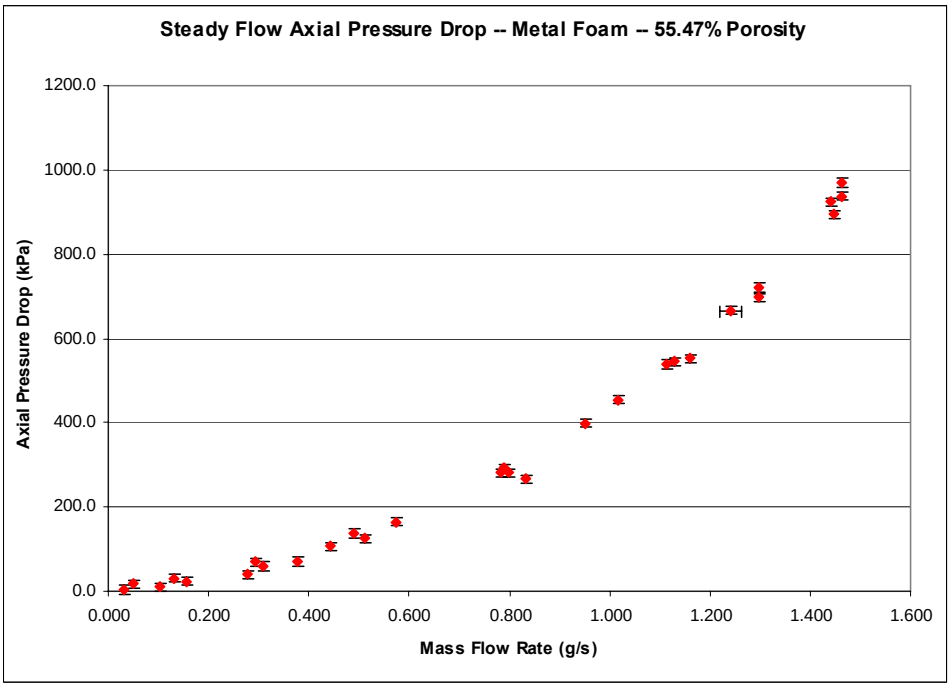

Figure 15: Steady Flow Axial Pressure Drop for SS Metal Foam

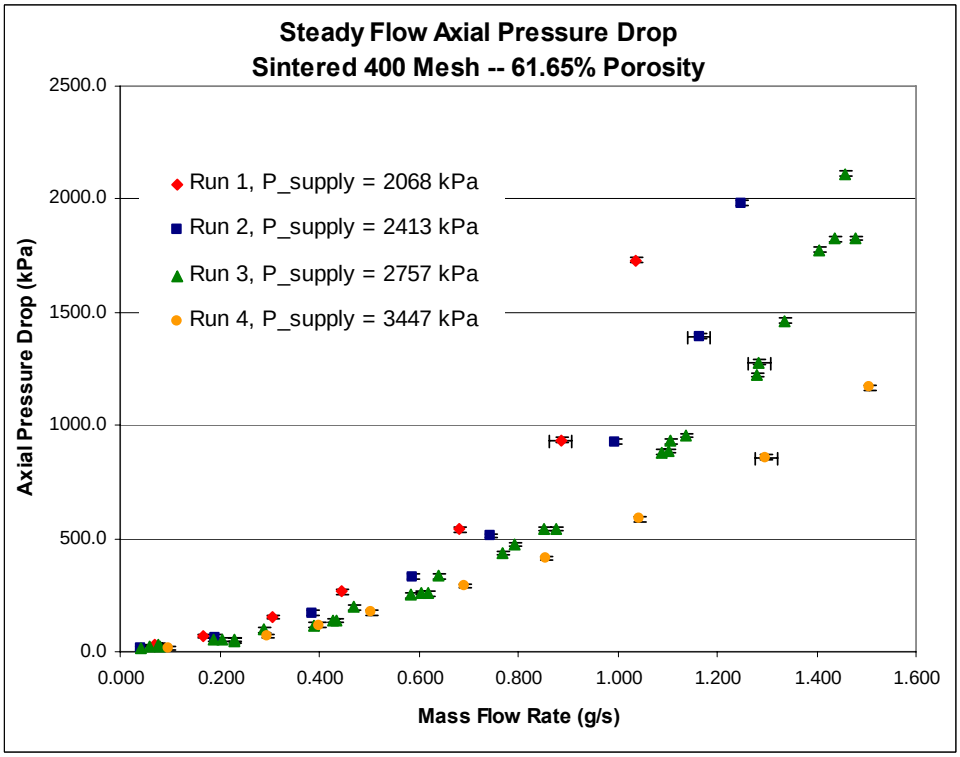

Figure 16: Steady Flow Axial Pressure Drop for Sintered 400 Mesh

Both the stainless steel metal foam sample and the sintered 400 mesh screen sample were at significantly lower porosities than the stacked wire mesh samples and resulted in higher pressure drops. Despite having a higher porosity than the metal foam sample, the sintered 400 mesh sample resulted in the highest change in pressure of all the tested materials. In fact, the flow resistance was so great that the full scale mass flow rate of 1.5 g/s was not achievable with a 300 psia (2068 kPa) regulator pressure. Therefore, additional data were recorded for higher regulator pressures, or supply pressures, of 350 psia, 400 psia, and 500 psia (2413 kPa, 2757 kPa, and 3447 kPa).

Figure 16 shows that, for a given porosity, the pressure drop is a function of both the mass flow rate and the initial supply pressure at the inlet of the porous region. For any given mass flow rate, the pressure drop across the porous medium was less for larger supply pressures. It appears as if the inertial effects have a smaller effect on the pressure drop across the porous sample for larger supply pressures based on the tendency toward a more linear relationship between the pressure drop and the mass flow rate as the supply pressure is increased. One contributor to this observed phenomenon is the increased effect of compressibility as pressure and density gradients across the porous zone are increased.

Harvey analytically showed that the friction factor for 1-D compressible flow is a function of pressure [30]. However, it remains unclear whether or not the results presented here imply that the hydrodynamic parameters, D and C, and thus the permeability and the Forchheimer coefficient are also functions of pressure. In order to investigate and account for the effects of compressibility in the presence of very large pressure gradients, Fluent simulations of the flow with varying supply pressures were

conducted to determine how hydrodynamic parameters are affected. The results are discussed later in this report.

Figure 17 shows the pressure drop test results for the stacked perforated nickel disks at 26.8% porosity. These structures provide a much lower pressure drop than the other tested samples. However, while the hydrodynamic losses are minimal, the challenge is to achieve a sufficiently high gas-to-matrix heat transfer in such a regenerator.

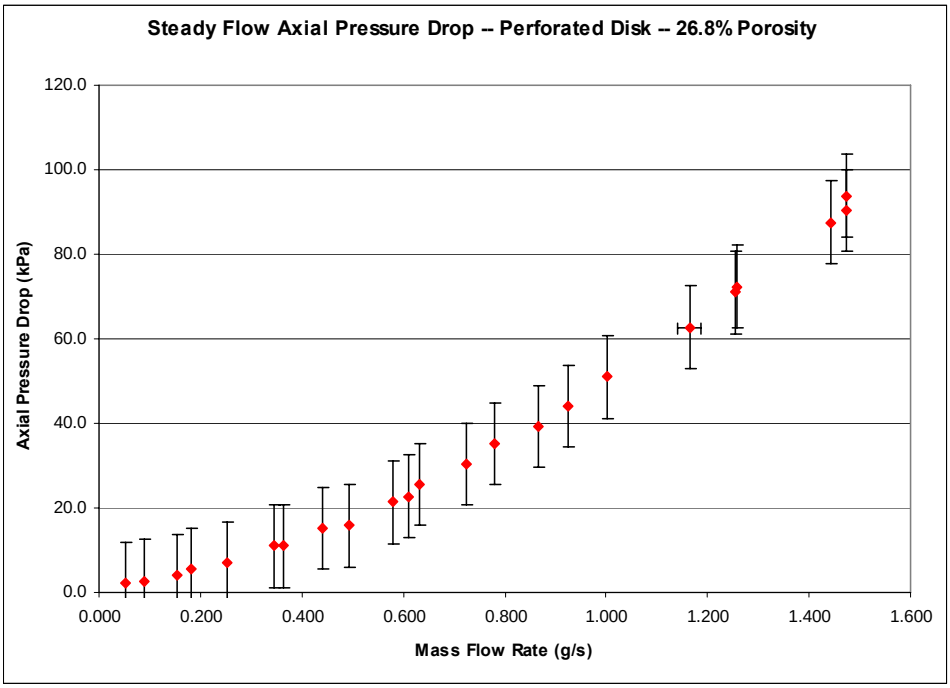

Figure 17: Steady Flow Axial Pressure Drop for Stacked Perforated Nickel Disks

The measured pressure drop for the perforated disks was typically over an order of magnitude smaller than that of the metal foam and the sintered mesh samples. While the results exhibited good repeatability, it should be noted that the error associated with the pressure transducers for the perforated disks was very high relative to the magnitude

of the pressure drop. This large relative error also applies to the pressure drops across the other samples at very low flow rates.

The tabulated data for all of these tests are provided in Appendix B. The empirical measurements of the mass flow rate and the outlet pressure are necessary and sufficient to close and solve the governing system of volume-averaged conservation equations. The measured quantities will be incorporated directly into the CFD model as boundary conditions thus allowing the system to be numerically solved for any given value of the viscous resistance, D, and the inertial resistance, C.

CHAPTER 4

COMPUTATIONAL METHOD

Modern computational fluid dynamics tools allow researchers to predict solutions of the governing conservation equations for flow fields that would otherwise be impractical to accurately solve. For the purposes of this investigation, the entire regenerator test section was modeled based on its exact dimensions and used along with the previously measured boundary conditions and user defined values of the relevant hydrodynamic parameters to obtain a full simulated model of the flow behavior throughout the porous test section. The simulated pressure drop across the porous medium could then be adjusted to match the actual pressure drop based on the assigned values of the viscous and inertial resistances.

4.1 Test Section CFD Model

The first step in creating the CFD model was to accurately model the exact geometry of the test section being used to conduct the experiments. Based on the internal dimensions of every component located between Pressure Transducer 1 and Pressure Transducer 2, the axisymmetric model shown in Figure 18 was created using Gambit modeling software. The location of each vertex is defined in Table 1 and the definition of each boundary and region is defined in Table 2.

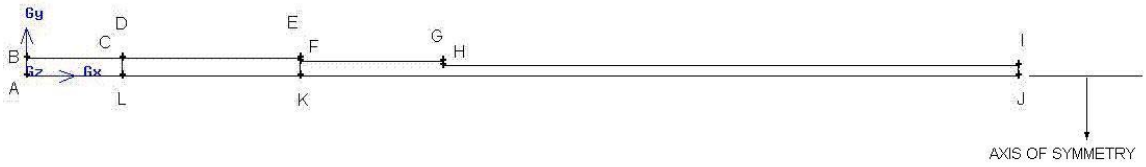

Figure 18: Regenerator Test Section Model without Meshing

Table 1: Regenerator Test Section Vertex Locations

Vertex	X Location (in)	X Location (cm)	Y Location (in)	Y Location (cm)
A	0.00000	0.00000	0.00000	0.00000
B	0.00000	0.00000	0.15000	0.38100
C	0.80000	2.03200	0.15000	0.38100
D	0.80000	2.03200	0.15625	0.39688
E	2.30000	5.84200	0.15625	0.39688
F	2.30000	5.84200	0.12500	0.31750
G	3.50000	8.89000	0.12500	0.31750
H	3.50000	8.89000	0.09000	0.22860
I	8.35000	21.20900	0.09000	0.22860
J	8.35000	21.20900	0.00000	0.00000
K	2.30000	5.84200	0.00000	0.00000
L	0.80000	2.03200	0.00000	0.00000

Table 2: Regenerator Test Section Boundary and Region Definitions

Boundary / Region	Definition
Line AB	Mass Flow Inlet
Line BC	Wall
Line CD	Wall
Line DE	Wall
Line EF	Wall
Line FG	Wall
Line GH	Wall
Line HI	Wall
Line IJ	Pressure Outlet
Line JKLA	Axis of Symmetry
Region ABCL	Fluid Zone 1
Region KFGHIJ	Fluid Zone 1
Region LCDEFK	Fluid Zone 2

The model was then meshed with a nodal spacing of 0.015” (0.381 cm) in the Y direction and a nodal spacing of 0.03” (0.0762 cm) in the X direction resulting in a total node count of about 2200. This meshing scheme was later compared to a much finer meshing scheme with twice as many nodes and it was concluded that the course mesh model performed 400% faster without significant loss in solution accuracy.

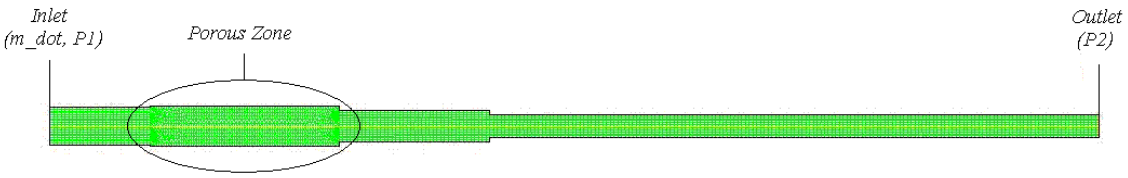

Figure 19: Regenerator Test Section Model with Meshing

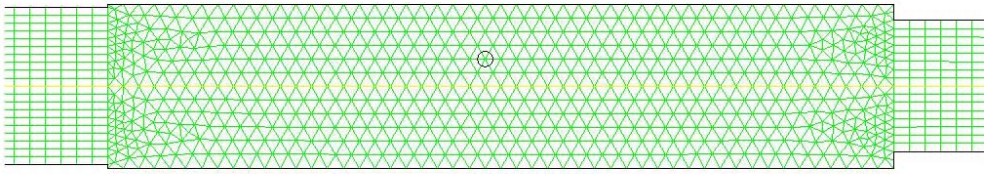

Figure 20: Regenerator Test Section Porous Zone Meshing

Upon successful meshing of the test section model, the file was exported to Fluent where the problem could be fully defined. The model was scaled in terms of SI units and the solver was set to solve a steady flow, axisymmetric, laminar model in terms of the physical velocity. Note that it was later determined that turbulent effects had a negligible effect on the simulated solution. Helium was selected as the working fluid and defined as a compressible ideal gas, steel was selected as the regenerator matrix material, and the convergence criteria for continuity, x-velocity, y-velocity, and energy

residuals were then set to 1.0e-7. Fluid Zone 2, or the regenerator volume, was defined as a porous zone where initial isotropic values for the viscous and inertial resistances, D and C, were guessed and inputted into the model. The model was then completely defined except for the two required boundary conditions. These boundary conditions, the mass flow rate, $\dot{m}$, and the gage pressure, $P2$, at the outlet, were defined based on the experimental values of a representative sample of the data reported in section 3.3.

4.2 CFD Results and Analysis

Because of the slight variation in experimental data from run to run, it proved useful to fit a 5th order polynomial to the data and use it to represent an average experimental pressure drop as a function of mass flow rate. Then using the measured $\dot{m}$ and $P2$ of a few representative data points within the set as boundary conditions, simulations were run in which the simulated values of the inlet pressure, $P1$, were sought.

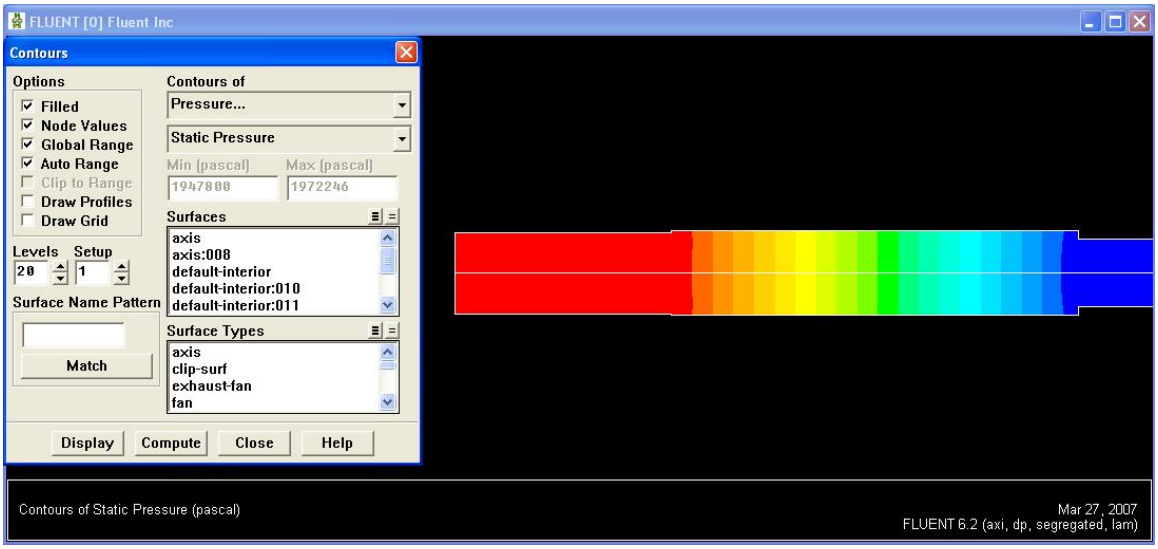

Figure 21: Pressure Contours Across Regenerator Test Section

The simulated pressure drop was then plotted versus the mass flow rate and a 5^{th} order polynomial fit to that data was compared to the experimental polynomial curve. The maximum percent difference between the curves for the range of 0 g/s to 1.5 g/s was then calculated and used as an indication of agreement between the simulation and the experimental data. By adjusting the Fluent defined viscous resistance, D, and the inertial resistance, C, and reiterating the simulation, the maximum percent error was reduced until acceptable agreement between simulation and experimentation was reached. It should be noted that the maximum percent error between the experimental and simulated curves consistently occurred at very low flow rates. Due to the inaccuracy of the pressure transducers at the very low pressure magnitudes associated with these low flow rates, more confidence was placed in models exhibiting good agreement between simulation and experimentation at flow rates higher than about 0.3 g/s. After numerous iterations, the values of D and C providing the best simulation performance could be used to calculate the permeability, Forchheimer coefficient, and friction factor associated with the steady flow of helium through the porous sample under investigation using equations 20, 21, and 23.

Table 3 summarizes the steady flow, axial hydrodynamic parameters for the various porous media often used as regenerator material for cryocooler refrigerators. Table 4 summarizes the periodic flow parameters for identical porous structures reported by Cha [29].

Table 3: Steady Flow Axial Hydrodynamic Parameters for Cryocooler Regenerator Structures for P_{supply} = 300 psia

Regenerator Material	Porosity (%)	D (1/m^2)	C (1/m)	K (m^2)	cf (-)
400 Mesh	69.69	2.77E+10	73000	1.753E-11	0.452
325 Mesh	69.69	2.35E+10	47000	2.067E-11	0.316
400 Sintered	61.65	5.55E+10	260000	6.848E-12	1.452
Metal Foam	55.47	2.65E+10	99000	1.161E-11	0.988
Perforated Disk	26.80	2.30E+10	115000	3.123E-12	5.279

Table 4: Periodic Flow Axial Hydrodynamic Parameters for Cryocooler Regenerator Structures for P_{charge} = 400 psia [Cha, 2007]

Regenerator Material	Porosity (%)	D (1/m^2)	C (1/m)	K (m^2)	Cf (-)
400 Mesh	69.20	3.9533E+10	120000	1.211E-11	0.630
325 Mesh	69.20	1.5565E+10	67000	3.077E-11	0.561
400 Sintered	62.00	5.0433E+10	110000	7.622E-12	0.637
Metal Foam	55.47	2.6533E+10	66000	1.160E-11	0.658
Perforated Disk	26.80	2.5000E+10	192000	2.873E-12	8.453

A direct comparison of the axial hydrodynamic parameters for helium flow through the porous samples indicates that, with the exception of the sintered 400 mesh and metal foam samples, the viscous and inertial resistances for steady flow are generally lower than those determined for periodic flow. For the sintered 400 mesh and metal foam samples, the inertial resistances were much greater for steady flow. It is believed that the absence of a general trend when comparing periodic to steady flow parameters is a result of differences in the solid matrix structures. These differences can be attributed to the randomness and the complete irregularity of the pores in the metal foam and sintered samples which obstruct flow more when compared the stacked screens and perforated disks and can significantly affect flow in the Forchheimer regime.

The uniqueness of the values reported in Table 3 and the sensitivity of the simulated pressure drop with respect to the hydrodynamic parameters can be seen in

Figure 22. For the sintered 400 mesh sample, multiple simulations were conducted for many different combinations of D and C. For each of these cases, the average percent difference between the simulated pressure drop and the actual pressure drop were calculated.

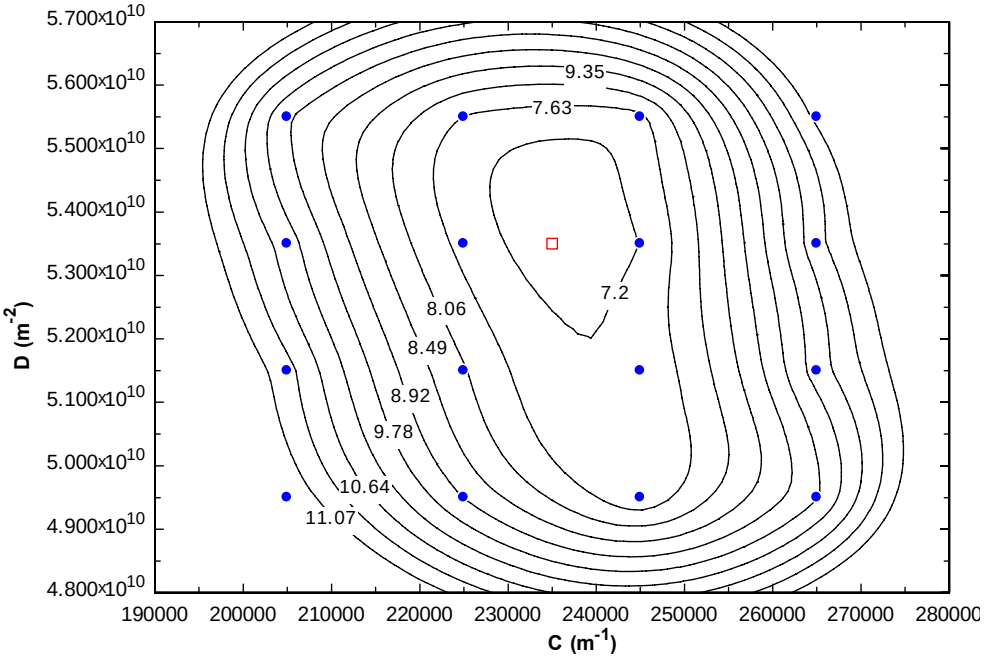

Figure 22: Average Percent Difference Contours (%) vs. D and C for Sintered 400 mesh

The red square in Figure 22 represents the steady flow viscous and inertial resistances for sintered 400 mesh as reported in Table 3. Each one of the blue points represents subsequent simulations that were performed using varying values of the hydrodynamic parameters. It can be seen that there is a local minimum which represents the values of D and C that would result in the smallest percent difference between simulation and experimentation. Therefore, it can be concluded that, for the range of D and C shown in Figure 22, there will exist unique values of the hydrodynamic parameters that will provide the most accurate prediction. The sensitivity of the CFD

model to changing D and C can also be seen on this plot. For the sintered 400 mesh sample, the viscous resistance may be varied by about ±3% and the inertial resistance may be varied by about ±5% without significantly changing the accuracy of the simulation.

These hydrodynamic parameters can also be expressed in non-dimensional terms. Figure 23 is the steady flow friction factor, f, as defined by Eq. 23 for all of the samples at the stated porosity. The average density in porous section was used to calculate Re_K and f.

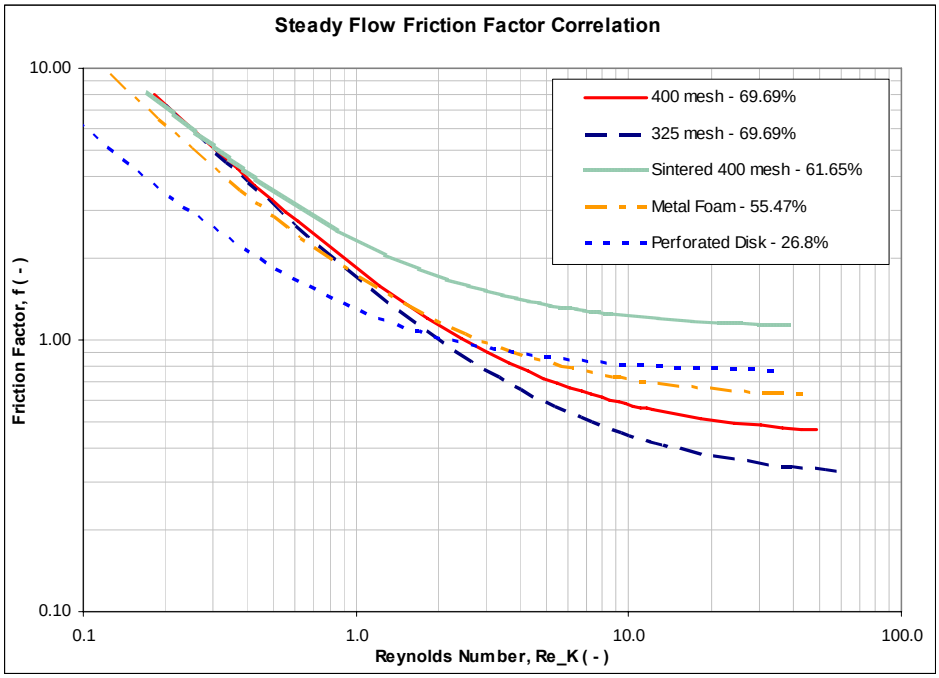

Figure 23: Steady Flow Axial Friction Factor for P_{supply} = 300 psia

Figures 24 - 28 show the experimental pressure drop across the porous test section as a function of mass flow rate of helium gas as well as the simulated pressure drop across an identical porous section using both the steady flow hydrodynamic

parameters and the periodic flow hydrodynamic parameters listed in Table 3 and Table 4. The supply pressure, P_{supply}, was equal to 300 psia (2068 kPa) for all cases unless otherwise stated.

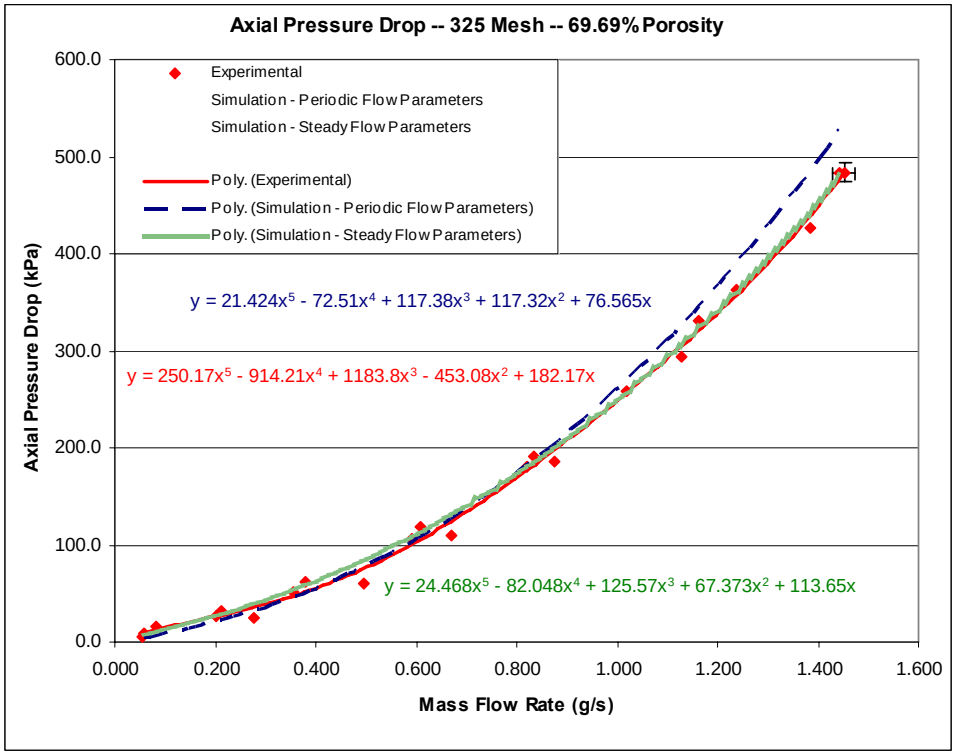

Figure 24: Simulated vs. Experimental Pressure Drop – 325 Mesh

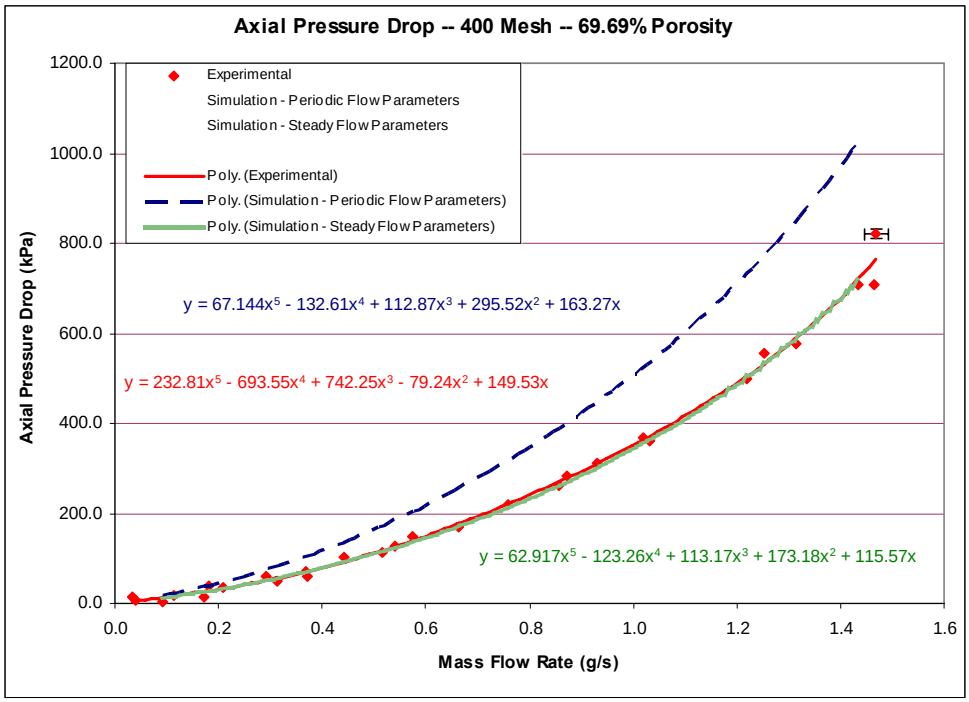

Figure 25: Simulated vs. Experimental Pressure Drop – 400 Mesh

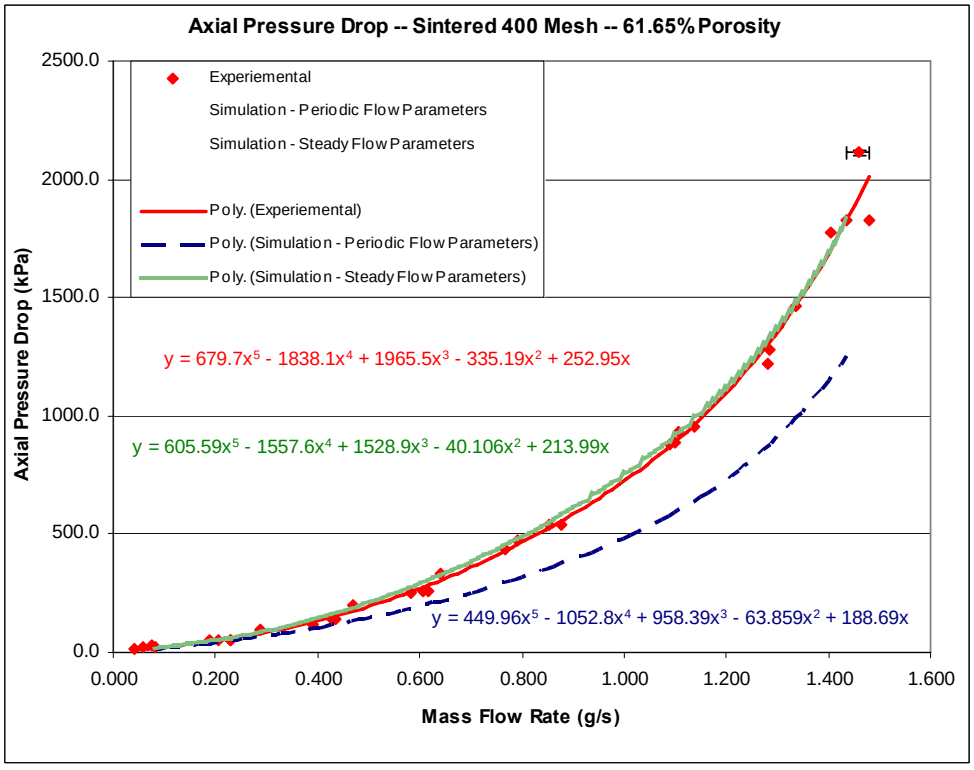

Figure 26: Simulated vs. Experimental Pressure Drop – Sintered 400 Mesh for P_{supply} = 400 psia (2758 kPa)

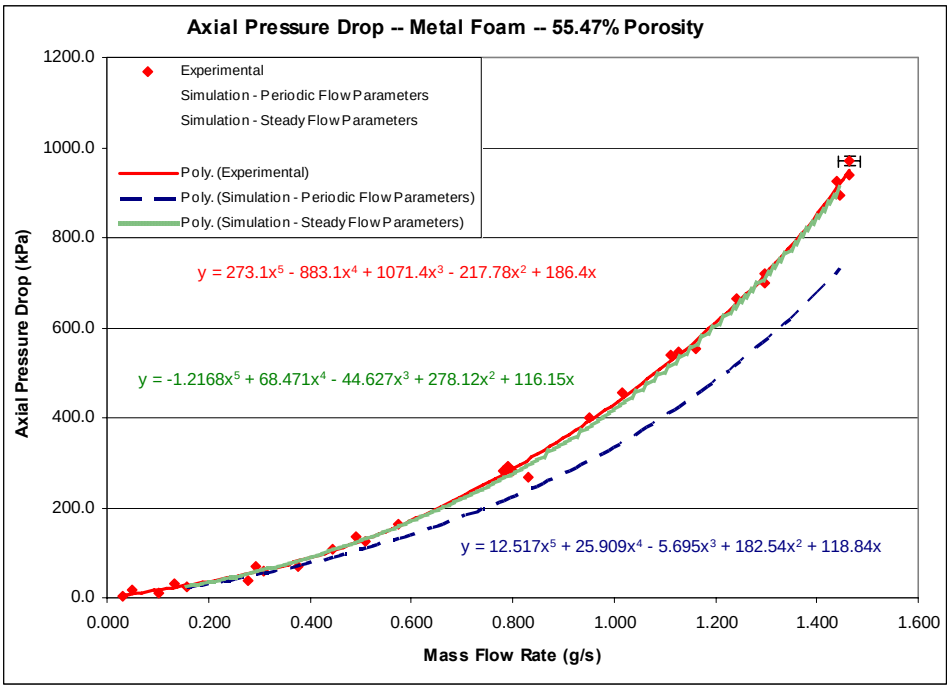

Figure 27: Simulated vs. Experimental Pressure Drop – Metal Foam

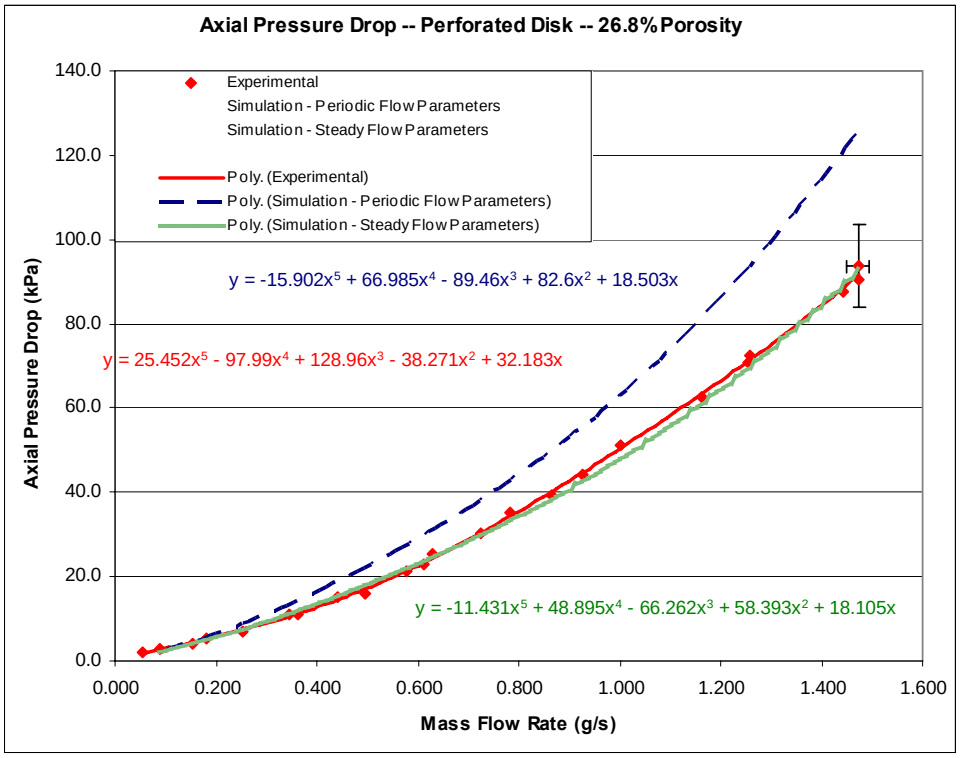

Figure 28: Simulated vs. Experimental Pressure Drop – Perforated Disk

The result of the smaller magnitude hydrodynamic parameters determined for steady flow through porous media is a significant under-prediction of the pressure drop across the regenerator volume for a given flow rate when compared to the predictions using periodic flow parameters. As previously mentioned, the exceptions to this observation were for the sintered 400 mesh sample and the metal foam sample where the steady flow pressure drop was greater than the periodic flow prediction for all flow rates. In all cases, it is clear that when comparing the magnitudes of the viscous resistance, D, and the inertial resistance, C, for steady and periodic flow, there can exist a very significant difference in how each set of parameters predicts the hydrodynamic losses. Data indicates that there can be a difference between the steady and periodic flow viscous resistance of as much as 42.6% while there can be a difference between the steady and periodic flow inertial resistance of as much as 57.7%. This conclusion suggests that using steady flow hydrodynamic parameters to predict behavior of periodic flow through porous media can lead to substantial solution inaccuracies.

For the sintered 400 mesh sample, the viscous and inertial resistance was correlated using data taken with a supply pressure of 400 psia. In order to examine the effects on the pressure drop of varying the supply pressure, multiple Fluent simulations were run using the data collected for supply pressures equal to 300 psia, 350 psia, 400 psia, and 500 psia (2068 kPa, 2413 kPa, 2757 kPa, and 3447 kPa). Each of these simulations assumed that the hydrodynamic parameters are constant with respect to the supply pressure. Using the same hydrodynamic parameters determined for P_{supply} = 400 psia, it can be seen in Figure 29 that at supply pressures less than 400 psia the

simulated pressure drops were less than the experimental values. For pressures greater than 400 psia, the simulations over-predicted the pressure drop.

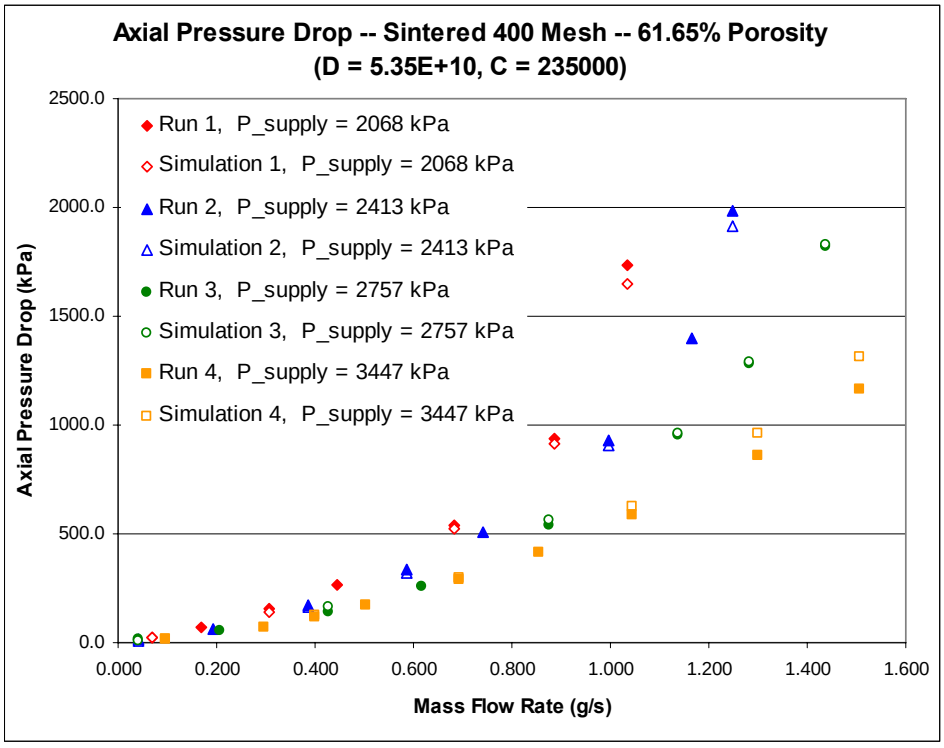

Figure 29: Simulation vs. Experimental Pressure Drop Using Constant Hydrodynamic Parameters

In order to correct for pressure variations and improve simulation performance, it is proposed that the following expressions for the adjusted steady flow viscous resistance, D_p, and the adjusted steady flow inertial resistance, C_p, be used to vary the hydrodynamic parameters based on the average of the inlet and outlet pressures in the porous region:

$$D_p = D_0 \left(\frac{P_{average}}{P_{critical}} \right)^{n_1} \qquad \text{(Eq. 31)}$$

$$C_p = C_0 \left(\frac{P_{average}}{P_{critical}} \right)^{n_2} \quad \text{(Eq. 32)}$$

where D_0 = 6.650E+10 m^{-2}, n_1 = -0.08, C_0 = 356000 m^{-1}, and n_2 = -0.21. The hydrodynamic parameters are now not only functions of the porous medium, but they are also functions of the average pressure in the porous medium, $P_{average}$, the critical pressure of the working fluid, $P_{critical}$, and constants D_0, n_1, C_0, and n_2. These constants were iteratively determined by seeking the minimum average error between the adjusted hydrodynamic parameters as calculated by Eq. 31 and Eq. 32 and the actual parameters determined through simulations fit to the experimental data. These constants are unique to the sintered 400 mesh sample that was tested.

Figure 30 shows that these adjusted parameters provided more accurate results for varying magnitudes of average pressure, especially at higher flow rates, when used to simulate the pressure drop across the porous sample. For both Run 1 and Run 4, the error at the maximum measured flow rate was reduced by a factor of four.

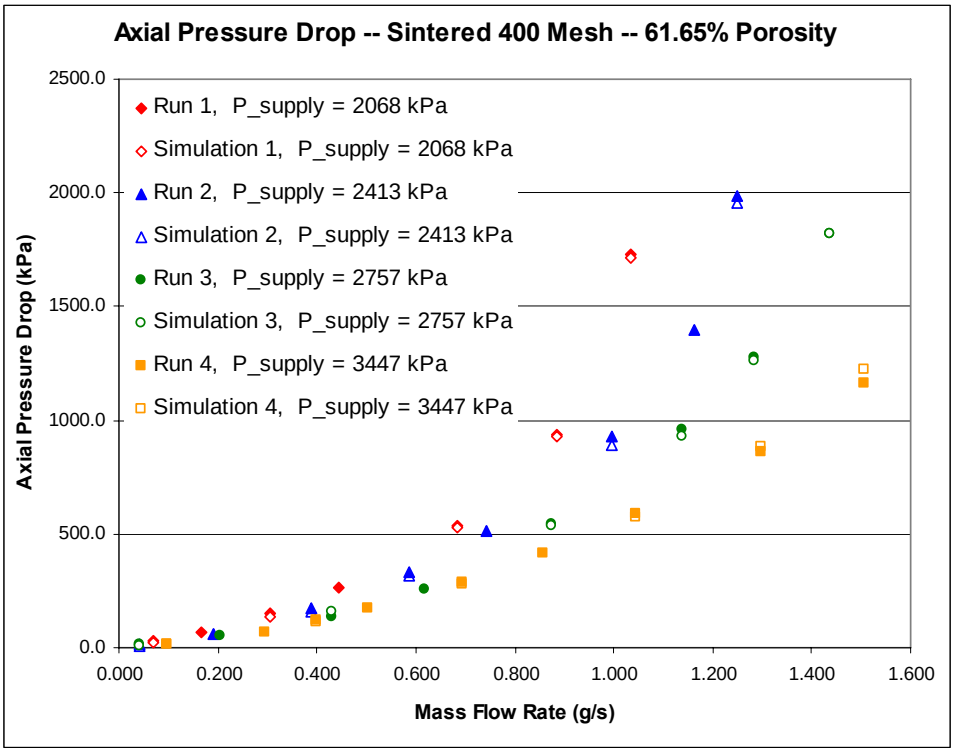

Figure 30: Simulation vs. Experimental Pressure Drop Using Pressure Dependant Hydrodynamic Parameters

Based on these findings, it can be concluded that the steady flow friction factor is not only a function of the Reynolds number, but also a function of pressure. While this study was only concerned with steady flow, the findings could be quite relevant to researchers dealing with cryogenic refrigerators as it implies that the operating pressure, or charge pressure, of these periodic systems could impact the friction factors previously associated with oscillatory flow through porous media.

Another common assumption used in the analysis of cryocooler regenerators is that of isotropic hydrodynamic parameters. While this assumption may be perfectly valid for certain structures like metal foam, for commonly used regenerator fillers like stacked mesh screens, one would expect these parameters to be quite different in the radial direction than they are in the axial direction. The effects of these differences can often be neglected for porous cryocooler components with large length-to-diameter ratios, or

aspect ratios, but as the diameter of these components increases in scale relative to the lengths, the isotropic regenerator assumption is no longer valid. In his report on the anisotropic hydrodynamic parameters of common regenerator structures, Cha presented the radial permeability and Forchheimer coefficient for a stacked 325 mesh porous medium at 69.6% porosity [21]. Table 5 compares this data with the axial data presented in this investigation while Figure 31 offers a comparison of the anisotropic friction factors.

Table 5: Anisotropic Hydrodynamic Parameters for 325 mesh

Regenerator Material	Porosity (%)	D (1/m^2)	C (1/m)	K (m^2)	Cf (-)
325 Mesh, Axial Direction	69.69	2.35E+10	47000	2.966E-11	0.263
325 Mesh, Radial Direction	69.60	6.80E+09	98600	1.4705E-10	1.234

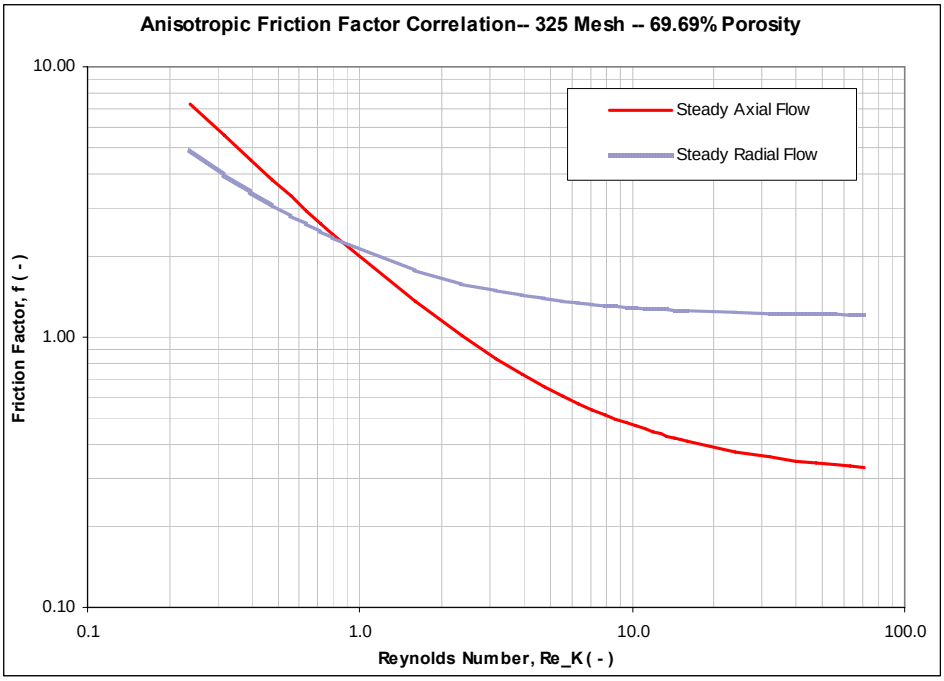

Figure 31: Anisotropic Steady Flow Friction Factor for 325 Mesh

CHAPTER 5

CONCLUSION

Due to the complex nature and micro-scale of porous components used in today's cryogenic refrigerators, it has proved very difficult to accurately predict the impact of the solid-fluid interactions within the porous media for periodic flow. In order to simplify the analysis of these periodic systems, researchers have often evaluated flow through components like the cryocooler regenerator assuming external drag losses based on isotropic hydrodynamic parameters associated with steady flow while neglecting the convective acceleration of the flow and the Brinkman effect. While these assumptions have made porous media flow analysis much easier, current computational fluid dynamic tools now allow researchers to quickly and accurately solve the volume-averaged governing fluid dynamics equations without making any of these simplifying assumptions.

In this investigation, Fluent CFD software was used to obtain and empirically correlate the steady flow axial permeability and Forchheimer coefficients associated with some common cryocooler regenerator structures at well-defined porosities in terms of relevant dimensionless parameters. These structures included stacked 325 mesh screens, stacked 400 mesh screens, sintered 400 mesh screens, metal foam, and stacked perforated disks. Based on experimental data, it was verified that the dimensionless friction factor based on the hydrodynamic parameters is not only a function of the Reynolds number, but it is also a function of pressure. It was also concluded that the hydrodynamic parameters themselves are functions of pressure. As a result, the correlations reported in this thesis are in the form of a power law based on a ratio of the average pressure in the porous region and the critical pressure of the working fluid.

This investigation also directly compared the steady flow and periodic flow viscous and inertial resistances for identical porous structures. Using these CFD tools, it was demonstrated how simulated hydrodynamic losses associated with steady helium flow though various porous media can be significantly different depending on whether steady flow parameters or periodic flow parameters were used in the governing momentum equation. Based on these results, it can be concluded that the behavior of periodic flow within the porous cryocooler regenerator cannot be accurately predicted based on steady flow hydrodynamic parameters. Likewise, the anisotropic parameters for a single porous sample were reported. Especially for components with small aspect ratios where multi-dimensional flow effects become more prevalent, it is important to note that the radial and axial friction factor can be significantly different and must be accounted for when analyzing porous components of the cryogenic refrigerator.

CHAPTER 6

RECOMMENDATIONS FOR FUTURE WORK

One of the main objectives of this investigation was to accurately determine and document the axial steady flow hydrodynamic parameters for some common cryocooler regenerator materials. During the process, it was discovered that these parameters are not only functions of the Reynolds number as is commonly assumed, but that they are also functions of pressure. For the sintered 400 mesh sample at a set porosity, multiple tests were conducted at varying supply pressures and the steady flow parameter correlations based on the average pressure were determined. Based on these findings, it is recommended that pressure dependant correlations be determined for all porous samples as it appears that compressibility effects can significantly change the value of the steady flow friction factor.

Additional testing is also recommended for each porous structure at varying porosities. This study focused on porous samples at well defined porosities in order to allow for direct comparison to identical structures used in previous periodic and anisotropic investigations. Based on the governing momentum equation, it is clear that increased porosity for any given sample will decrease the magnitude of the steady flow pressure drop, but it is unclear whether or not varying the porosity for the same porous structure will significantly affect the permeability or Forchheimer coefficient. If these parameters are affected, the porosity should be included along with the pressure and Reynolds number in the steady flow friction factor correlations.

Ultimately, the intention of this study is to help researchers make more appropriate assumptions regarding the analysis of periodic systems involving porous media flow like in cryogenic refrigerators. Therefore, the conclusions presented in this thesis need to be verified on a system level. It is recommended that the effect of

assuming steady flow hydrodynamic parameters for the many porous regions of the cryocooler be quantified using a periodic CFD model of the entire system. Likewise, the validity of assuming isotropic hydrodynamic parameters should be determined through simulation by comparing results to models using both the axial and radial parameters. A system level parametric study could determine the appropriateness of these common assumptions.

Finally, it should be remembered that cryogenic refrigerators operate at cryogenic temperatures. All of the experimental data reported in this investigation were gathered at room temperature and it is therefore recommended that similar experiments be conducted for steady flow pressure drop through porous media at cryogenic temperatures for the purpose of confirming the conclusions presented in this report under actual operating conditions.

APPENDIX A: EXPERIMENTAL PROCEDURE

TEST

Axial Steady Flow Pressure Drop Test

Location: Georgia Institute of Technology - Love Building Room 241 - Fluids Laboratory

Spring 2007

OBJECTIVE

The purpose if this experiment is to determine the axial steady flow pressure drop for various cryocooler regenerator materials at pre-determined porosities. The pressure drop across the regenerator test section will be recorded for each porous sample for a range of mass flow rates from 0 g/s to 1.5 g/s of helium gas.

APPARATUS

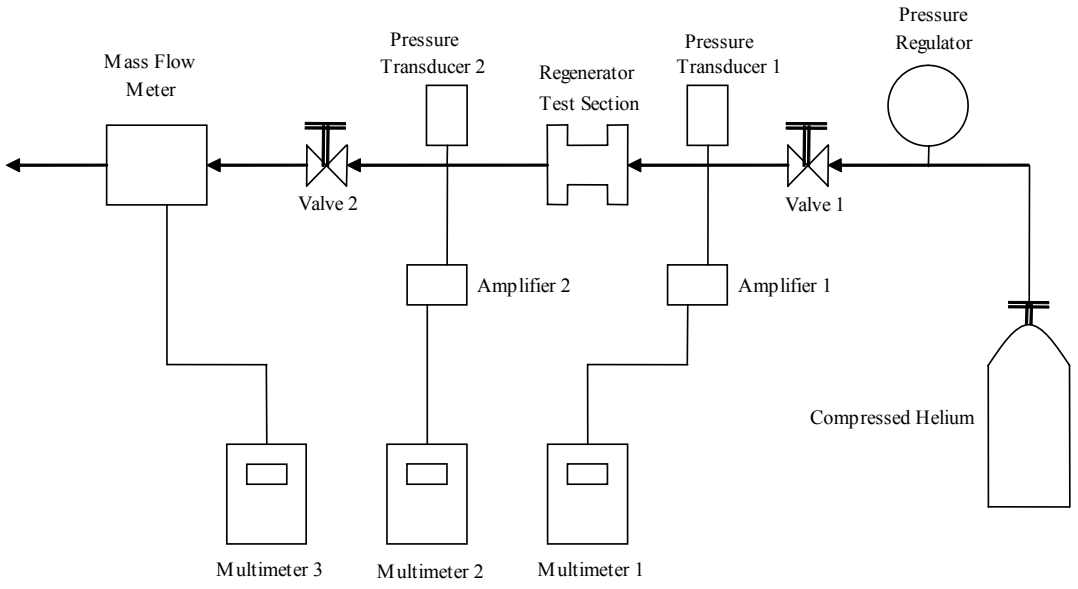

EQUIPMENT AND MATERIALS

Porous regenerator samples:

- Stacked stainless steel 325 mesh screens at 69.69% porosity
- Stacked stainless steel 400 mesh screens at 69.69% porosity
- Sintered stainless steel 400 mesh screens at 61.65% porosity
- Stainless steel Metal Foam at 55.47% porosity
- Stacked perforated nickel disks at 26.8% porosity

Two Paine Electronics high frequency pressure transducers:

- Calibrated for pressure range of 0 psia to 400 psia
- Accuracy: 0.25% F.S. max, where for:
  - Pressure Transducer 1: F.S. = 400 psia
  - Pressure Transducer 2: F.S. = 400 psia
  - Total Uncertainty of pressure drop measurement: ±9.8 kPa
- Repeatability: within 0.05% F.S.

Sierra Instruments analog mass flow mater:

- Calibrated for helium gas a atmospheric pressure and temperature
- Accuracy: 1.5% F.S. max, where F.S. = 1.5 g/s
- Total Uncertainty of mass flow rate measurement: ±0.0225 g/s

PROCEDURE

Prior to testing, calibrate pressure transducers for pressures up to 400 psia and fill the regenerator test section with the porous sample being tested. Close the test section and ensure that the test apparatus is leak tight, by capping the line after the mass flow meter and charging the line to 500 psia. Monitor the output of the two pressure transducers to make sure a leak does not exist at any point within the apparatus.

Once the test apparatus is deemed leak tight, remove the cap after the mass flow meter thus opening the line to the atmosphere. Close valve 2 and completely open valve 1. Adjust the regulator to provide a supply pressure of 300 psia. Slowly open valve 2 just enough to initiate gas flow through the test apparatus. Record the voltage outputs (V1, V2, V3) from multimeters 1, 2, and 3. Open valve 2 slightly more to increase the mass flow rate. At this flow rate, record V1, V2, and V3. Repeat this procedure until data is collected for eight to ten mass flow rates along regular intervals between 0 g/s and 1.5 g/s. Perform three runs or more as needed. Repeat experiment for all porous samples.

DATA PROCESSING

Use the following equations to calculate the mass flow rate, inlet pressure (P1), outlet pressure (P2), and pressure drop where V1, V2, and V3 are measured in volts, the mass flow rate is in units of g/s, and the pressures are in units of kPa:

$$\dot{m} = 0.3 \cdot V3 \qquad \text{(Eq. 1)}$$

$$P1 = 689.48 \cdot V1 \qquad \text{(Eq. 2)}$$

$$P2 = 689.48 \cdot V2 \quad \text{(Eq. 3)}$$

$$dP = P1 - P2 \quad \text{(Eq. 4)}$$

For each set of data, plot the pressure drop as a function of mass flow rate.

APPENDIX B: TABULATED EXPERIMENTAL DATA AND RESULTS

Appendix B.1: 400 Mesh Pressure Drop Data

400 SS Mesh Regenerator Pressure Drop Test -- 69.69% Porosity

Mass Flow Meter Calibration Conditions

Pc =	15.000	psiaa
Tc =	294.000	K

Experimental Conditions

T =	300.000	K	27.0	C

Regenerator Volume:

Porosity =	0.6969
Diameter (in) =	0.3125
Diameter (m) =	7.938E-03
CS Area (in^2) =	0.0767
CS Area (m^2) =	4.9483E-05
Length (in) =	1.500
Length (m) =	0.0381
Total Volume (m^3) =	1.8853E-06
Solid Volume (m^3) =	5.7136E-07
Mass (g) =	4.588
Avg Wire Diameter (in) =	1.455E-3
Avg Wire Diameter (m) =	3.696E-5
D (1/m^2) =	2.770E+10
C (1/m) =	73000

Properties of Helium

Viscosity (kg/m-s) =	1.990E-05
Density (kg/m^3) =	1.625E-01

Properties of Stainless Steel (AISI 304)

Density (kg/m^3) =	8030

Pressure Transducer Uncertainty -- 0.25% of Full Scale

	Full Scale (psia)	Uncertainty (psia)	Uncertainty (kPa)
P.T. 1	400.0	1.0	6.9
P.T. 2	400.0	1.0	6.9

Pressure Drop Uncertainty (kPa) = 9.8

Mass Flow Rate Uncertainty -- 1.5% of Full Scale

Full Scale (g/s)	Uncertainty (g/s)
1.5	0.0225

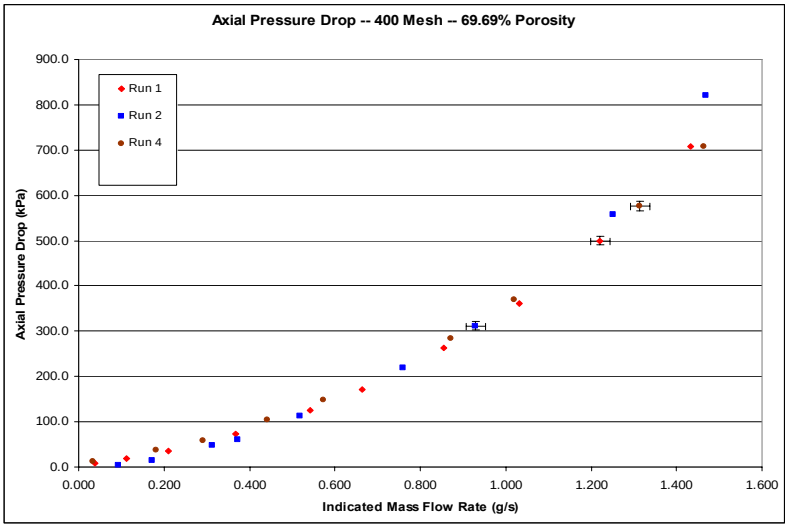

	V1 (V)	V2 (V)	V3 (V)	P1 (psia)	P2 (psia)	P1 (kPa)	P2 (kPa)	M* (g/s)	dP (kPa)
RUN 1	3.143	3.131	0.128	314.3	313.1	2167.0	2158.8	0.039	8.3
	3.097	3.070	0.376	309.7	307.0	2135.3	2116.7	0.113	18.6
	3.051	3.000	0.698	305.1	300.0	2103.6	2068.4	0.209	35.2
	2.984	2.879	1.227	298.4	287.9	2057.4	1985.0	0.368	72.4
	2.923	2.740	1.806	292.3	274.0	2015.4	1889.2	0.542	126.2
	2.882	2.633	2.213	288.2	263.3	1987.1	1815.4	0.664	171.7
	2.825	2.444	2.853	282.5	244.4	1947.8	1685.1	0.856	262.7
	2.770	2.245	3.436	277.0	224.5	1909.9	1547.9	1.031	362.0
	2.707	1.982	4.069	270.7	198.2	1866.4	1366.5	1.221	499.9
	2.637	1.611	4.779	263.7	161.1	1818.2	1110.8	1.434	707.4
RUN 2	3.117	3.110	0.309	311.7	311.0	2149.1	2144.3	0.093	4.8
	3.071	3.050	0.574	307.1	305.0	2117.4	2102.9	0.172	14.5
	3.000	2.930	1.044	300.0	293.0	2068.4	2020.2	0.313	48.3
	2.968	2.880	1.241	296.8	288.0	2046.4	1985.7	0.372	60.7
	2.905	2.740	1.724	290.5	274.0	2002.9	1889.2	0.517	113.8
	2.816	2.498	2.533	281.6	249.8	1941.6	1722.3	0.760	219.3
	2.746	2.294	3.098	274.6	229.4	1893.3	1581.7	0.930	311.6
	2.601	1.793	4.172	260.1	179.3	1793.3	1236.2	1.252	557.1
	2.473	1.282	4.895	247.3	128.2	1705.1	883.9	1.469	821.2
RUN 3	2.920	2.902	0.113	292.0	290.2	2013.3	2000.9	0.034	12.4
	2.860	2.804	0.601	286.0	280.4	1971.9	1933.3	0.180	38.6
	2.822	2.737	0.971	282.2	273.7	1945.7	1887.1	0.291	58.6
	2.794	2.644	1.472	279.4	264.4	1926.4	1823.0	0.442	103.4
	2.773	2.558	1.912	277.3	255.8	1911.9	1763.7	0.574	148.2
	2.732	2.320	2.903	273.2	232.0	1883.7	1599.6	0.871	284.1
	2.712	2.177	3.400	271.2	217.7	1869.9	1501.0	1.020	368.9
	2.675	1.839	4.380	267.5	183.9	1844.4	1268.0	1.314	576.4
	2.655	1.628	4.880	265.5	162.8	1830.6	1122.5	1.464	708.1

Appendix B.2: 325 Mesh Pressure Drop Data

325 SS Mesh Regenerator Pressure Drop Test -- 69.69% Porosity

Mass Flow Meter Calibration Conditions

Pc =	15.000	psiaa
Tc =	294.000	K

Experimental Conditions

T =	300.000	K	27.0	C

Regenerator Volume:

Porosity =	0.6969
Diameter (in) =	0.3125
Diameter (m) =	7.938E-03
CS Area (in^2) =	0.0767
CS Area (m^2) =	4.9483E-05
Length (in) =	1.500
Length (m) =	0.0381
Total Volume (m^3) =	1.8853E-06
Solid Volume (m^3) =	5.714E-07
Mass (g) =	4.588
Avg Wire Diameter (in) =	1.653E-3
Avg Wire Diameter (m) =	4.20E-5
D (1/m^2) =	2.350E+10
C (1/m) =	47000

Properties of Helium

Viscosity (kg/m-s) =	1.990E-05
Density (kg/m^3) =	1.625E-01

Properties of Stainless Steel (AISI 304)

Density (kg/m^3) =	8030

Pressure Transducer Uncertainty -- 0.25% of Full Scale

	Full Scale (psia)	Uncertainty (psia)	Uncertainty (kPa)
P.T. 1	400.0	1.0	6.9
P.T. 2	400.0	1.0	6.9

Pressure Drop Uncertainty (kPa) = 9.8

Mass Flow Rate Uncertainty -- 1.5% of Full Scale

Full Scale (g/s)	Uncertainty (g/s)
1.5	0.0225

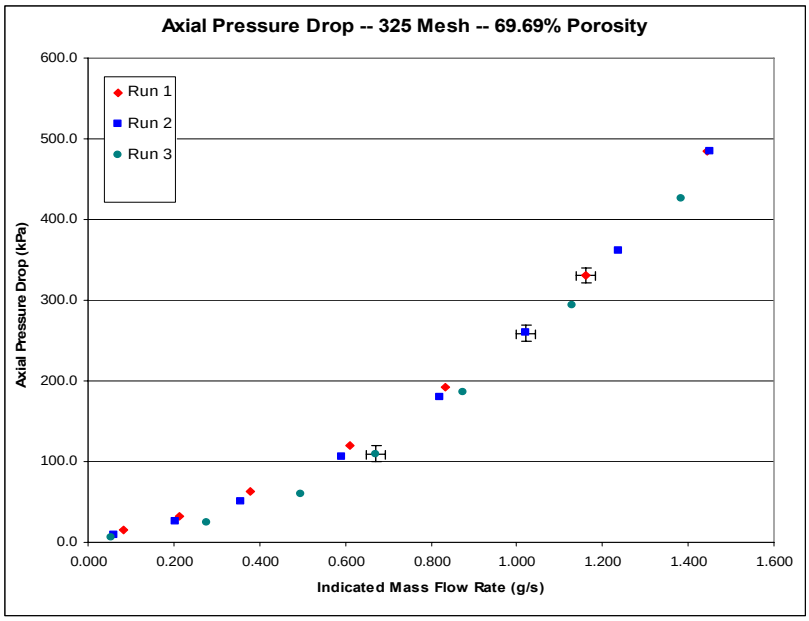

	V1 (V)	V2 (V)	V3 (V)	P1 (psia)	P1 (kPa)	P2 (psia)	P2 (kPa)	M* (g/s)	dP (kPa)
RUN 1	2.898	2.876	0.277	289.8	1998.1	287.6	1982.9	0.083	15.2
	2.858	2.812	0.706	285.8	1970.5	281.2	1938.8	0.212	31.7
	2.824	2.733	1.262	282.4	1947.1	273.3	1884.3	0.379	62.7
	2.786	2.613	2.032	278.6	1920.9	261.3	1801.6	0.610	119.3
	2.754	2.476	2.778	275.4	1898.8	247.6	1707.2	0.833	191.7
	2.707	2.227	3.870	270.7	1866.4	222.7	1535.5	1.161	331.0
	2.669	1.967	4.810	266.9	1840.2	196.7	1356.2	1.443	484.0
RUN 2	2.904	2.891	0.198	290.4	2002.2	289.1	1993.3	0.059	9.0
	2.863	2.825	0.675	286.3	1974.0	282.5	1947.8	0.203	26.2
	2.830	2.756	1.187	283.0	1951.2	275.6	1900.2	0.356	51.0
	2.787	2.632	1.967	278.7	1921.6	263.2	1814.7	0.590	106.9
	2.750	2.489	2.733	275.0	1896.1	248.9	1716.1	0.820	180.0
	2.716	2.340	3.400	271.6	1872.6	234.0	1613.4	1.020	259.2
	2.684	2.159	4.120	268.4	1850.6	215.9	1488.6	1.236	362.0
	2.652	1.950	4.840	265.2	1828.5	195.0	1344.5	1.452	484.0
RUN 3	2.918	2.910	0.181	291.8	2011.9	291.0	2006.4	0.054	5.5
	2.865	2.829	0.927	286.5	1975.4	282.9	1950.5	0.278	24.8
	2.820	2.733	1.649	282.0	1944.3	273.3	1884.3	0.495	60.0
	2.780	2.621	2.237	278.0	1916.8	262.1	1807.1	0.671	109.6
	2.735	2.465	2.921	273.5	1885.7	246.5	1699.6	0.876	186.2
	2.690	2.264	3.760	269.0	1854.7	226.4	1561.0	1.128	293.7
	2.648	2.029	4.610	264.8	1825.7	202.9	1399.0	1.383	426.8

Appendix B.3: Sintered 400 Mesh Pressure Drop Data

Sintered 400 SS Mesh Regenerator Pressure Drop Test -- 61.65% Porosity

Mass Flow Meter Calibration Conditions

Pc =	15.000	psiaa
Tc =	294.000	K

Experimental Conditions

T =	300.000	K	27.0	C

Regenerator Volume:

Porosity =	0.6165
Diameter (in) =	0.3125
Diameter (m) =	7.938E-03
CS Area (in^2) =	0.0767
CS Area (m^2) =	4.9483E-05
Length (in) =	1.500
Length (m) =	0.0381
Total Volume (m^3) =	1.8853E-06
Solid Volume (m^3) =	7.2304E-07
Mass (g) =	5.806
D (1/m^2) =	5.550E+10
C (1/m) =	260000

Properties of Helium

Viscosity (kg/m-s) =	1.990E-05
Density (kg/m^3) =	1.625E-01

Properties of Stainless Steel (AISI 304)

Density (kg/m^3) =	8030

Pressure Transducer Uncertainty -- 0.25% of Full Scale

	Full Scale (psia)	Uncertainty (psia)	Uncertainty (kPa)
P.T. 1	400.0	1.0	6.9
P.T. 2	400.0	1.0	6.9

Pressure Drop Uncertainty (kPa) = 9.8

Mass Flow Rate Uncertainty -- 1.5% of Full Scale

Full Scale (g/s)	Uncertainty (g/s)
1.5	0.0225

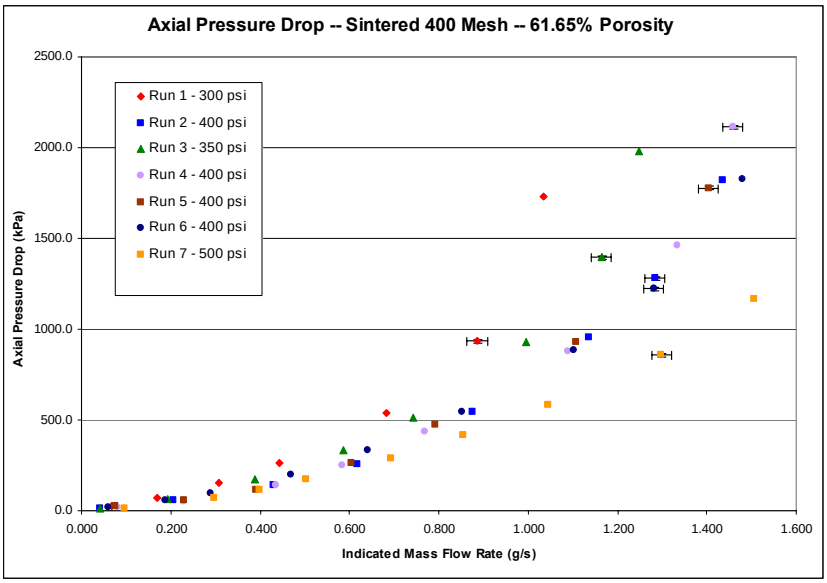

	V1 (V)	V2 (V)	V3 (V)	P1 (psia)	P2 (psia)	P1 (kPa)	P2 (kPa)	M* (g/s)	dP (kPa)
RUN 1	2.886	2.847	0.230	288.6	284.7	1989.8	1962.9	0.069	26.9
	2.857	2.755	0.561	285.7	275.5	1969.8	1899.5	0.168	70.3
	2.827	2.605	1.021	282.7	260.5	1949.2	1796.1	0.306	153.1
	2.805	2.422	1.479	280.5	242.2	1934.0	1669.9	0.444	264.1
	2.779	1.996	2.276	277.9	199.6	1916.1	1376.2	0.683	539.9
	2.761	1.405	2.952	276.1	140.5	1903.7	968.7	0.886	934.9
	2.751	0.240	3.450	275.1	24.0	1896.8	165.5	1.035	1731.3
RUN 2	3.940	3.920	0.135	394.0	392.0	2716.6	2702.8	0.041	13.8
	3.900	3.820	0.687	390.0	382.0	2689.0	2633.8	0.206	55.2
	3.850	3.650	1.430	385.0	365.0	2654.5	2516.6	0.429	137.9
	3.810	3.436	2.059	381.0	343.6	2626.9	2369.1	0.618	257.9
	3.760	2.974	2.920	376.0	297.4	2592.4	2050.5	0.876	541.9
	3.730	2.344	3.790	373.0	234.4	2571.8	1616.1	1.137	955.6
	3.710	1.855	4.280	371.0	185.5	2558.0	1279.0	1.284	1279.0
	3.690	1.045	4.790	369.0	104.5	2544.2	720.5	1.437	1823.7
RUN 3	3.440	3.417	0.139	344.0	341.7	2371.8	2356.0	0.042	15.9
	3.390	3.298	0.642	339.0	329.8	2337.3	2273.9	0.193	63.4
	3.350	3.102	1.291	335.0	310.2	2309.8	2138.8	0.387	171.0
	3.310	2.828	1.958	331.0	282.8	2282.2	1949.8	0.587	332.3
	3.290	2.549	2.477	329.0	254.9	2268.4	1757.5	0.743	510.9
	3.260	1.914	3.320	326.0	191.4	2247.7	1319.7	0.996	928.0
	3.240	1.217	3.880	324.0	121.7	2233.9	839.1	1.164	1394.8
	3.230	0.354	4.160	323.0	35.4	2227.0	244.1	1.248	1982.9
	V1 (V)	V2 (V)	V3 (V)	P1 (psia)	P2 (psia)	P1 (kPa)	P2 (kPa)	M* (g/s)	dP (kPa)
RUN 4	3.950	3.920	0.270	395.0	392.0	2723.4	2702.8	0.081	20.7
	3.900	3.830	0.763	390.0	383.0	2689.0	2640.7	0.229	48.3
	3.860	3.660	1.451	386.0	366.0	2661.4	2523.5	0.435	137.9

	3.830	3.469	1.943	383.0	346.9	2640.7	2391.8	0.583	248.9
	3.790	3.156	2.563	379.0	315.6	2613.1	2176.0	0.769	437.1
	3.730	2.452	3.630	373.0	245.2	2571.8	1690.6	1.089	881.2
	3.700	1.577	4.450	370.0	157.7	2551.1	1087.3	1.335	1463.8
	3.680	0.615	4.860	368.0	61.5	2537.3	424.0	1.458	2113.3
RUN 5	3.970	3.930	0.256	397.0	393.0	2737.2	2709.7	0.077	27.6
	3.910	3.830	0.768	391.0	383.0	2695.9	2640.7	0.230	55.2
	3.870	3.700	1.304	387.0	370.0	2668.3	2551.1	0.391	117.2
	3.820	3.441	2.017	382.0	344.1	2633.8	2372.5	0.605	261.3
	3.780	3.094	2.643	378.0	309.4	2606.2	2133.3	0.793	473.0
	3.720	2.372	3.690	372.0	237.2	2564.9	1635.4	1.107	929.4
	3.670	1.094	4.680	367.0	109.4	2530.4	754.3	1.404	1776.1
RUN 6	3.910	3.880	0.199	391.0	388.0	2695.9	2675.2	0.060	20.7
	3.860	3.780	0.628	386.0	378.0	2661.4	2606.2	0.188	55.2
	3.830	3.690	0.964	383.0	369.0	2640.7	2544.2	0.289	96.5
	3.780	3.495	1.563	378.0	349.5	2606.2	2409.7	0.469	196.5
	3.740	3.257	2.137	374.0	325.7	2578.7	2245.6	0.641	333.0
	3.690	2.902	2.841	369.0	290.2	2544.2	2000.9	0.852	543.3
	3.640	2.355	3.670	364.0	235.5	2509.7	1623.7	1.101	886.0
	3.610	1.836	4.270	361.0	183.6	2489.0	1265.9	1.281	1223.1
	3.560	0.910	4.930	356.0	91.0	2454.5	627.4	1.479	1827.1
RUN 7	4.680	4.660	0.325	468.0	466.0	3226.8	3213.0	0.098	13.8
	4.630	4.530	0.989	463.0	453.0	3192.3	3123.3	0.297	68.9
	4.610	4.440	1.332	461.0	444.0	3178.5	3061.3	0.400	117.2
	4.590	4.340	1.677	459.0	434.0	3164.7	2992.3	0.503	172.4
	4.560	4.140	2.309	456.0	414.0	3144.0	2854.4	0.693	289.6
	4.540	3.940	2.852	454.0	394.0	3130.2	2716.6	0.856	413.7
	4.520	3.670	3.480	452.0	367.0	3116.4	2530.4	1.044	586.1
	4.480	3.235	4.330	448.0	323.5	3088.9	2230.5	1.299	858.4
	4.460	2.769	5.020	446.0	276.9	3075.1	1909.2	1.506	1165.9

Appendix B.4: Metal Foam Pressure Drop Data

SS Metal Foam Regenerator Pressure Drop Test -- 55.47% Porosity

Mass Flow Meter Calibration Conditions

Pc =	15.000 psiaa	
Tc =	294.000 K	

Experimental Conditions

T =	300.000 K	27.0 C

Regenerator Volume:

Porosity =	0.5547
Diameter (in) =	0.3125
Diameter (m) =	7.938E-03
CS Area (in^2) =	0.0767
CS Area (m^2) =	4.9483E-05
Length (in) =	1.500
Length (m) =	0.0381
Total Volume (m^3) =	1.8853E-06
Solid Volume (m^3) =	8.3948E-07
Mass (g) =	6.741
D (1/m^2) =	2.650E+10
C (1/m) =	99000

Properties of Helium

Viscosity (kg/m-s) =	1.990E-05
Density (kg/m^3) =	1.625E-01

Properties of Stainless Steel (AISI 304)

Density (kg/m^3) =	8030

Pressure Transducer Uncertainty -- 0.25% of Full Scale

	Full Scale (psia)	Uncertainty (psia)	Uncertainty (kPa)
P.T. 1	400.0	1.0	6.9
P.T. 2	400.0	1.0	6.9

Pressure Drop Uncertainty (kPa) = 9.8

Mass Flow Rate Uncertainty -- 1.5% of Full Scale

Full Scale (g/s)	Uncertainty (g/s)
1.5	0.0225

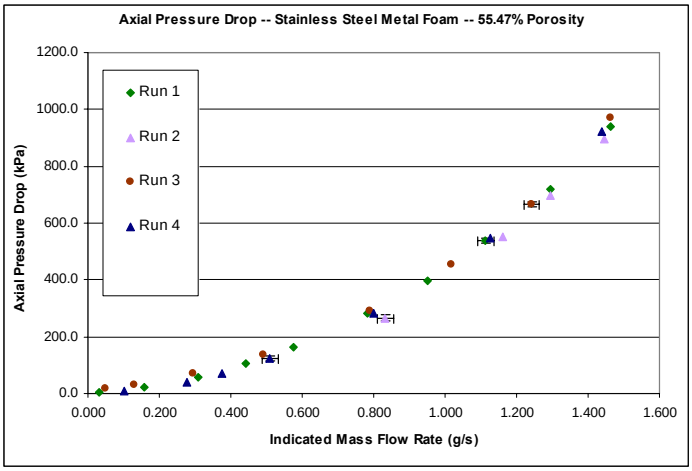

	V1 (V)	V2 (V)	V3 (V)	P1 (psia)	P1 (kPa)	P2 (psia)	P2 (kPa)	M* (g/s)	dP (kPa)
RUN 1	2.937	2.932	0.107	293.7	2025.0	293.2	2021.6	0.032	3.4
	2.892	2.858	0.521	289.2	1994.0	285.8	1970.5	0.156	23.4
	2.854	2.768	1.025	285.4	1967.8	276.8	1908.5	0.308	59.3
	2.832	2.677	1.479	283.2	1952.6	267.7	1845.7	0.444	106.9
	2.817	2.578	1.916	281.7	1942.3	257.8	1777.5	0.575	164.8
	2.798	2.391	2.610	279.8	1929.2	239.1	1648.5	0.783	280.6
	2.784	2.205	3.170	278.4	1919.5	220.5	1520.3	0.951	399.2
	2.766	1.985	3.710	276.6	1907.1	198.5	1368.6	1.113	538.5
	2.748	1.703	4.320	274.8	1894.7	170.3	1174.2	1.296	720.5
	2.733	1.373	4.880	273.3	1884.3	137.3	946.7	1.464	937.7
RUN 2	2.793	2.406	2.774	279.3	1925.7	240.6	1658.9	0.832	266.8
	2.744	1.943	3.870	274.4	1891.9	194.3	1339.7	1.161	552.3
	2.732	1.720	4.320	273.2	1883.7	172.0	1185.9	1.296	697.8
	2.716	1.419	4.820	271.6	1872.6	141.9	978.4	1.446	894.3
RUN 3	2.940	2.914	0.162	294.0	2027.1	291.4	2009.1	0.049	17.9
	2.910	2.865	0.438	291.0	2006.4	286.5	1975.4	0.131	31.0
	2.870	2.769	0.978	287.0	1978.8	276.9	1909.2	0.293	69.6
	2.830	2.631	1.633	283.0	1951.2	263.1	1814.0	0.490	137.2
	2.780	2.355	2.631	278.0	1916.8	235.5	1623.7	0.789	293.0
	2.740	2.081	3.390	274.0	1889.2	208.1	1434.8	1.017	454.4
	2.698	1.732	4.140	269.8	1860.2	173.2	1194.2	1.242	666.0
	2.662	1.255	4.880	266.2	1835.4	125.5	865.3	1.464	970.1
RUN 4	2.917	2.902	0.343	291.7	2011.2	290.2	2000.9	0.103	10.3
	2.864	2.806	0.927	286.4	1974.7	280.6	1934.7	0.278	40.0
	2.840	2.737	1.256	284.0	1958.1	273.7	1887.1	0.377	71.0
	2.813	2.632	1.700	281.3	1939.5	263.2	1814.7	0.510	124.8
	2.763	2.356	2.663	276.3	1905.0	235.6	1624.4	0.799	280.6
	2.707	1.916	3.760	270.7	1866.4	191.6	1321.0	1.128	545.4
	2.656	1.316	4.800	265.6	1831.3	131.6	907.4	1.440	923.9

Appendix B.5: Perforated Disk Pressure Drop Data

Mass Flow Meter Calibration Conditions

Pc =	15.0 psiaa	
Tc =	294.0 K	

Experimental Conditions

T =	273.0 K	27.0 C

Regenerator Volume:

Porosity =	0.2680
Diameter (in) =	0.5900
Diameter (m) =	1.499E-02
CS Area (in^2) =	0.2734
CS Area (m^2) =	1.7639E-04
Length (in) =	1.500
Length (m) =	0.0381
Total Volume (m^3) =	6.7203E-06
Solid Volume (m^3) =	
Mass (g) =	
D (1/m^2) =	2.300E+10
C (1/m) =	115000

Properties of Helium

Viscosity (kg/m-s) =	1.990E-05
Density (kg/m^3) =	1.625E-01

Properties of Stainless Steel (AISI 304)

Density (kg/m^3) =	8030

Pressure Transducer Uncertainty -- 0.25% of Full Scale

	Full Scale (psia)	Uncertainty (psia)	Uncertainty (kPa)
P.T. 1	400.0	1.0	6.9
P.T. 2	400.0	1.0	6.9

Pressure Drop Uncertainty (kPa) = 9.8

Mass Flow Rate Uncertainty -- 1.5% of Full Scale

Full Scale (g/s)	Uncertainty (g/s)
1.5	0.0225

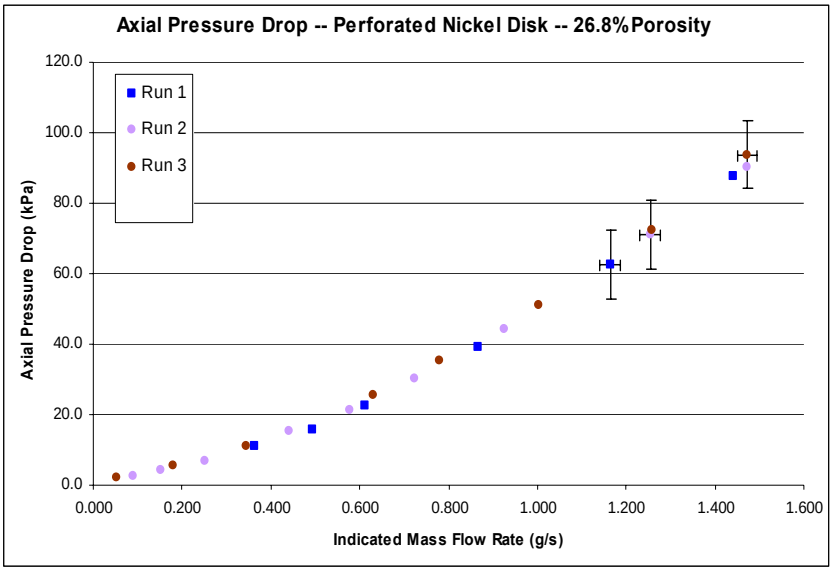

	V1 (V)	V2 (V)	V3 (V)	P1 (psia)	P1 (kPa)	P2 (psia)	P2 (kPa)	M* (g/s)	dP (kPa)
RUN 1									
	2.878	2.862	1.208	287.8	1984.3	286.2	1973.3	0.362	11.0
	2.850	2.827	1.648	285.0	1965.0	282.7	1949.2	0.494	15.9
	2.828	2.795	2.035	282.8	1949.8	279.5	1927.1	0.611	22.8
	2.778	2.721	2.887	277.8	1915.4	272.1	1876.1	0.866	39.3
	2.723	2.632	3.880	272.3	1877.5	263.2	1814.7	1.164	62.7
	2.670	2.543	4.810	267.0	1840.9	254.3	1753.3	1.443	87.6
RUN 2	2.981	2.977	0.298	298.1	2055.3	297.7	2052.6	0.089	2.8
	2.953	2.947	0.511	295.3	2036.0	294.7	2031.9	0.153	4.1
	2.921	2.911	0.839	292.1	2014.0	291.1	2007.1	0.252	6.9
	2.872	2.850	1.470	287.2	1980.2	285.0	1965.0	0.441	15.2
	2.831	2.800	1.928	283.1	1951.9	280.0	1930.5	0.578	21.4
	2.793	2.749	2.412	279.3	1925.7	274.9	1895.4	0.724	30.3
	2.745	2.681	3.087	274.5	1892.6	268.1	1848.5	0.926	44.1
	2.666	2.563	4.180	266.6	1838.2	256.3	1767.1	1.254	71.0
	2.610	2.479	4.910	261.0	1799.5	247.9	1709.2	1.473	90.3
RUN 3	2.973	2.970	0.177	297.3	2049.8	297.0	2047.8	0.053	2.1
	2.931	2.923	0.602	293.1	2020.9	292.3	2015.4	0.181	5.5
	2.881	2.865	1.147	288.1	1986.4	286.5	1975.4	0.344	11.0
	2.792	2.755	2.102	279.2	1925.0	275.5	1899.5	0.631	25.5
	2.741	2.690	2.604	274.1	1889.9	269.0	1854.7	0.781	35.2
	2.676	2.602	3.340	267.6	1845.0	260.2	1794.0	1.002	51.0
	2.600	2.495	4.190	260.0	1792.6	249.5	1720.3	1.257	72.4
	2.536	2.400	4.910	253.6	1748.5	240.0	1654.8	1.473	93.8

REFERENCES

1 W.E. Gifford and R.C. Longsworth, “Pulse-Tube Refrigeration.” ASME paper no. 63-WA-290 presented at the Winter Annual Meeting in Philadelphia, PA. November 17-22, 1963.

2 W.E. Gifford and R.C. Longsworth, “Surface Heat Pumping.” Advances in Cryogenic Engineering, Vol. 11. Plenum Press, New York, pp. 171-179

3 R. Radebaugh, “Development of the Pulse Tube Refrigerator as an Efficient and Reliable Cryocooler,” National Institute of Standards and Technology. Submitted to: Proc. Institute of Refrigeration, London. 1999-2000

4 J.S. Cha, “CFD Simulation of Multi-Dimensional Effects in Inertance Tube Pulse Tube Cryocoolers,” Master’s Thesis, Georgia Institute of Technology, Atlanta, GA. 2004.

5 G. Walker, “Cryocoolers.” Plenum Press, New York. 1983.

6 Moran and Shapiro, “Fundamentals of Engineering Thermodynamics,” 4th Ed. Wiley and Sons, Inc. New York, 2000.

7 E.I. Mikulin, A.A. Tarasov, M.P. Shkrebyonock, “Low-Temperature Expansion Pulse Tubes.” Advances in Cryogenic Engineering, Vol. 29. Plenum Press, New York, 1984. pp. 629-637.

8 R. Radebaugh, J. Zimmerman, D.R. Smith, B. Louie, “A Comparison of Three Types of Pulse Tube Refrigerators: New Methods for Reaching 60 K.” Advances in Cryogenic Engineering, Vol. 31. Plenum Press, New York, 1986. pp. 779.

9 P.R. Roach, A. Kashani, “Pulse Tube Coolers with an Inertance Tube: Theory, Modeling, and Practice.” Advances in Cryogenic Engineering, Vol. 43. Plenum Press, New York, 1998. pp. 1895-1902

10 S.W. Zhu, S.L. Zhou, N. Yoshimura, Y. Matsubara, “Phase Shift Effect of the Long Neck Tube for the Pulse Tube Refrigerator.” Proceedings of the 9th International Cryocoolers Conference, Waterville Valley, New Hampshire. June 1996, pp. 269.

11 D.L. Gardner, G.W. Swift, “Use of Inertance in Orifice Pulse Tube Refrigerators.” Cryogenics, Vol. 37. Elsevier, 1997. pp. 117-121

12 W.E. Gifford, R.C. Longsworth, “Pulse Tube Refrigeration Progress.” Advances in Cryogenic Engineering, Vol. 10. Plenum Press, New York, 1964. pp. 69-79.

13 J.P. Harvey, “Parametric Study of Cryocooler Regenerator Performance.” Master’s Thesis, Georgia Institute of Technology, Atlanta, GA. 1999.

14 Pecharsky, Gechneidner, McCallum, Dennis, “Influence of Alloying on the Behavior and Properties and Er_3Ni.” Cryocooler 9, Plenum Press, New York and London, 1997. pp. 663

15 Bradshaw, Orlowska, Jewell, Jones, Scull, “Improvements to the Cooling Power of a Space Qualified Two-Stage Stirling Cycle Cooler.” Cryocoolers 9, Plenum Press, New York and London, 1997. pp. 79.

16 R.A. Ackermann, “Cryogenic Regenerative Heat Exchangers.” Plenum Press, New York and London, 1997.

17 Chafe, Green, Hendrix, “A Neodymium Plate Regenerator for Low-Temperature Gifford-McMahon Refrigerators.” Cryocoolers 9, Plenum Press, New York and London, 1997. pp. 653.

18 R. Radebaugh, M. Lewis, E. Luo, J.M. Pfotenhauer, G.F. Nellis, L.A. Schunk, “Inertance Tube Optimization for Pulse Tube Cryocoolers.” Advances in Cryogenic Engineering: Transactions of the Cryogenic Engineering Conference, Vol. 51, 2006. pp. 59-67.

19 Organ, “Thermodynamics and Gas Dynamics of the Stirling Cycle Machine.” Cambridge University Press, Cambridge, 1992.

20 K. Nam, S. Jeong, “Measurement of Cryogenic Regenerator Characteristics under Oscillating Flow and Pulsating Pressure.” Cryogenics 43, Elsevier, 2003. pp. 575-581.

21 J.S. Cha, S.M. Ghiaasiaan, P.V. Desai, “Measurement of Anisotropic Hydrodynamic Parameters of Pulse Tube or Stirling Regenerators.” Advances in Cryogenic Engineering: Transactions of the Cryogenic Engineering Conference, Vol. 51, 2006. pp. 1911-1918.

22 Jeong, Nam, Jung, “Regenerator Characterization under Oscillating Flow and Pulsating Pressure.” Cryocoolers 12, Kluwer Academic, New York, 2003. pp. 531.

23 D.A. Nield, A. Bejan, “Convection In Porous Media.” 2nd Edition, 1999. Springer, New York. pp. 1-22.

24 S. Whitaker, “The Forchheimer Equation: A Theoretical Development.” Transport in Porous Media 25. Kluwer Academic, 1996. pp. 27-61.

25 Y. Ishizaki, E. Ishizaki, H.R. Mueller, T. Ohtsuka, K. Hamaguchi, “Design of a New Type Regenerator.” Advances in Cryogenic Engineering, Vol. 45A. Kluwer Academic, 2000. pp. 345-348.

26 Y.K. Hou, Y.L. Ju, L.W. Yan, J.T. Liang, Y. Zhou, “Experimental Study on a High Frequency Miniature Pulse Tube Refrigerator with Inertance Tube.” Advances in Cryogenic Engineering: Proceedings of the Cryogenic Engineering Conference, Vol. 47A. American Institute of Physics, 2002. pp. 731-738.

27 “Fluent 6.2 User’s Guide.” January, 2005. Chapters 7 & 9.

28 "Handbook of Porous Media." 2nd Edition. K. Vafai, Editor. Taylor and Francis Group, 2005.

29 J.S. Cha, "Measurement And Correlation Of Anisotropic Hydrodynamic Parameters In Porous Media Under Steady And Oscillating Flow: Application To Cryocooler Regenerator." PHD Dissertation, Georgia Institute of Technology, Atlanta, GA. 2007.

30 J.P. Harvey, "Oscillatory Compressible Flow and Heat Transfer in Porous Media – Application to Cryocooler Regenerators." PHD Dissertation, Georgia Institute of Technology, Atlanta, GA. 2003.